FEDERAL UNIVERSITY OF SANTA CATARINA
TECHNOLOGY CENTER
AUTOMATION AND SYSTEMS DEPARTMENT
UNDERGADUATE COURSE IN CONTROL AND AUTOMATION ENGINEERING

Otávio Trentin

Coupling of Thermal and Mechanical Ball Screw Models for Machine Tools

Aachen
2020

Otávio Trentin

Coupling of Thermal and Mechanical Ball Screw Models for Machine Tools

Final report of the subject DAS5511 (Course Final Project) as a Concluding Dissertation of the Undergraduate Course in Control and Automation Engineering at the Federal University of Santa Catarina in Florianópolis.
Supervisor: Prof. Dr. Marcelo De Lellis Costa de Oliveira
Co-supervisor: Florian Kneer, M.Sc. RWTH.

Aachen
2020

Ficha de identificação da obra elaborada pelo autor,
através do Programa de Geração Automática da Biblioteca Universitária da UFSC.

Trentin, Otávio
Coupling of Thermal and Mechanical Ball Screw Models for Machine Tools / Otávio Trentin ; orientador, Marcelo De Lellis Costa de Oliveira, coorientador, Florian Kneer, 2020.
88 p.

Trabalho de Conclusão de Curso (graduação) - Universidade Federal de Santa Catarina, Centro Tecnológico, Graduação em Engenharia de Controle e Automação, Florianópolis, 2020.

Inclui referências.

1. Engenharia de Controle e Automação. 2. Ball Screw Drive. 3. Mathematical Model. 4. Thermo-Mechanical Coupling. I. Oliveira, Marcelo De Lellis Costa de. II. Kneer, Florian. III. Universidade Federal de Santa Catarina. Graduação em Engenharia de Controle e Automação. IV. Título.

Otávio Trentin

Coupling of Thermal and Mechanical Ball Screw Models for Machine Tools

This dissertation was evaluated in the context of the subject DAS5511 (Course Final Project) and approved in its final form by the Undergraduate Course in Control and Automation Engineering

Florianópolis, December 14, 2020.

Prof. Dr. Hector Bessa Silveira
Course Coordinator

Examining Board:

Prof. Dr. Marcelo De Lellis Costa de Oliveira
Advisor
UFSC/CTC/DAS

Florian Kneer, M.Sc. RWTH.
Supervisor
Laboratory for Machine Tools and Production Engineering/RWTH Aachen University

---

Ahryman S. Busse de Siqueira Nascimento
Evaluator
Labmetro/UFSC

Prof. Dr. Ricardo José Rabelo
Board President
UFSC/CTC/DAS

ABSTRACT

In machine tools, ball screw drives are the most widely used linear actuators due to their high efficiency and positioning accuracy. A ball screw drive is composed of a shaft with helical grooves, a nut system with helical grooves, and spheres between the nut system and the shaft. At the WZL a ball screw mechanical model has been developed for the calculation of the load distribution on the components and contact characteristics of the spheres. During the operation of the ball screw drive, friction will occur on the contacts of the spheres generating heat and resulting in an increase of the components' temperature. This thermal variation will result in thermal expansion changing the load distribution and contact characteristics in the system. In order to add the influence of these thermal variations to the existing mechanical model, a second model of ball screws was created to deal with the thermal problem. This work presents the contributions to the previously existing mechanical and thermal model and the development of the models' coupling. The model results are compared to the data measured on the test rig developed in previous work.

Keywords: ball screw drive, mathematical model, thermo-mechanical coupling.

RESUMO

Em máquinas ferramentas fusos de esferas recirculantes são os atuadores lineares mais utilizados devido a sua alta eficiência e precisão de posicionamento. Um fuso de esferas é composto por eixo com ranhuras helicoidais, castaneira com ranhuras helicoidais e esferas entre a castanheira e o eixo. No WZL um modelo mecânico de fusos de esferas foi desenvolvido para o cálculo de distrubuição de carga nos componentes e características de contato nas esferas. Durante a operação do sistema atrito ocorrerá nos contatos das esferas gerando calor e resultando em um aumento de temperatura nos componentes. Esta variação termal resultará em expansão térmica, alterando a distribuição de carga e as características de contato no sistema. Com o intuito de adicionar esta influência termal no modelo mecânico existente, um segundo modelo de fusos de esferas foi criado para lidar com o problema térmico. Este trabalho apresenta as contribuições no modelo mecânico e no modelo térmico previamente existentes e também o desenvolvimento do acoplamento de ambos. Os resultados obtidos são comparados a dados medidos na bancada de testes desenvolvida previamente.

Palavras-chave: fuso de esferas, modelo matemático, acoplamento termo-mecânico.

LIST OF FIGURES

LIST OF TABLES

LIST OF ABBREVIATIONS AND ACRONYMS

CSB	Coulomb Solid Body
DAQ	Data Acquisition System
EHD	Elastohydrodynamic
FEA	Finite Element Analysis
FEM	Finite Element Method
HMI	Human-Machine Interface
LVDT	Linear Variable Differential Transformer
MSPE	Mean Square Percentage Error
NUH	Non Updated Heat
PLC	Programmable Logic Controller
PSO	Particle Swarm Optimization
UH	Updated Heat
WZL	Laboratory for Machine Tools and Production Engineering

LIST OF SYMBOLS

Symbol	Description	Unit
Roman letters		
A	Cross Section Area	m^2
E	Young's Modulus	N/m^2
FB	Ball to Ball Forces	N
FP	Pressure Forces	N
FR	Hydrodynamic Rolling Forces	N
FS	Sliding Forces	N
F_N	Contact Normal Force	N
F_T	Thermal Forces	N
F_B	Rolling Friction Forces	N
$F_{Coulomb}$	Solid State Force Component for Rolling Friction	N
F_{EHD}	Fluid Force Component for Rolling Friction	N
F_{Fluid}	Fluid Friction Component	N
$F_{SolidBody}$	Solid Body Friction Component	N
F_{ao}	Preload Force	N
F	Friction Forces	N
G	Material Index Without Unit	–
K	Stiffness Matrix	N/m
L	Thermal Load Coefficient	–
MB	Ball to Ball Moment	Ns
MC	Curvature Friction Moment	Ns
MER	Elastic Resistance in Ball-Groove Contact	Ns
M_0	Speed Dependent Friction Torque	Nmm
M_1	Load Dependent Friction Torque	Nmm
M_A	Moment due to the irreversible deformation	Nm
M_C	Drilling Moment	Nm
M_{Aref}	Frictional Torque due to the irreversible deformation	Nm
M_{Bref}	Frictional Torque due to the Rolling	Nm
M_B	Moment due to the Rolling	Nm
$M_{Coulomb}$	Solid-Body Moment Component for Drilling Friction	Nm
M_{Cref}	Frictional Torque due to the Drilling	Nm
M_{EHD}	Fluid Moment Component for Drilling Friction	Nm
M_{rs}	Friction Torque of the deep groove ball bearings	Nmm
Mr_{bf}	Friction Torque on the Bearing in the Motor Side	Nm
Mr_{bs}	Friction Torque on the Bearing Opposite the Motor	Nm
Mr_n	Total Friction Torque of nut-screw interface	Nm

Symbol	Description	Unit
Nu_{Forced}	Nusselt Number for Forced Convection	–
Nu_{Free}	Nusselt Number for Free Convection	–
P_r	Prandtl Number	–
Q_{bf}	Heat Generation on the Bearing in the Motor Side	W
Q_{bs}	Heat Generation on the Bearing Opposite the Motor	W
Q_{ns}	Heat Generation of the nut-screw interface	W
Q_n	Heat Fraction Acting on the Nut	W
Q_s	Heat Fraction Acting on the Screw Shaft	W
R_a	Rayleigh Number	–
R_e	Reynolds Number	–
R_q	Roughness Of Components	m
R_x	Equivalent Radius in the Rolling Direction	m
R_y	Transversal Equivalent Radius	m
R	Replacement Radius of the Hertzian Theory	m
S_{sur}	Linear Speed of the Surface	m/s
U	Speed Index Without Unit	–
W	Load Index Without Unit	–
$\dot{Q}$	Heat Transfer Rate	W
$\dot{q}$	Heat Flux	W/m^2
$\sum F$	Sum of forces	N
A	Pure Stiffness Matrix	W/K
B	Area Matrix	m^2
MB	Heat Capacity Matrix	J/K
$\mathbf{T_r}$	Temperature of Nodes Column Matrix	K
u	Heat Flux Column Matrix	W/m^2
a	Major half axis of the contact ellipse in the Hertzian Theory	m
b	Minor half axis of the contact ellipse in the Hertzian Theory	m
d_0	Dimension of the Analysed Element in the Reynolds Number and Rayleigh Number Calculation	m
d_M	Bearing Diameter	mm
d_W	Groove Diameter	m
d_m	Screw Diameter	m
d_t	Temporal Increment	s

Symbol	Description	Unit
d	Distance from the Center of Contact and the Points where the Pure Rolling Happen	m
f_0	Coefficient for Speed Dependent Friction Torque	N
g	Gravity	m/s^2
h_{forced}	Heat Transfer Coefficient for Forced Convection	W/m^2K
h_{free}	Heat Transfer Coefficient for Free Convection	W/m^2K
$h_{isotherm}$	Lubricant Film Thickness Isotherm	m
h	Lubricant Film Thickness	m
i_B	Transmission Ratio of Drilling Speed and Bearing Speed	–
i_ω	Transmission Ratio between the Rolling Elements and the Axis of Rotation	–
k_{air}	Conductivity of the Air	W/mK
k	Raddi Ratio in Olaru Friction Model	–
n	Operation Speed	rpm
Greek letters		
ΔT	Difference of Temperature	K
Λ_{Factor}	Lubricating Film Density Factor	–
Λ	Lubricating Film Density	–
Φ_T	Thermal Reduction Factor	–
α_T	Thermal Expansion Coefficient	m/mK
α_{air}	Thermal Diffusivity of the Air	m^2/s
α	Contact angle	rad
β_{air}	Heat Expansion Coefficient of the Air	K^{-1}
δ	Displacement	m
$\eta(\nu, \rho)$	Viscosity Function of the Temperature and Pressure	Pas
κ	Damping Constant of the Rolling Element	–
λ_S	Lubrication parameter of the Stribeck Curve	–
λ_{heat}	Heat Transfer Coefficient	W/m^2K
λ	Percentage Factor of Frictions	–
$\mu_{Coulomb}$	Coulomb Friction Coefficient	–
μ_{EHD}	Fluid Friction Coefficient	–
μ_{Gleit}	Coulomb coefficient of friction for sliding friction	–
μ_{Hertz}	Hertz's Coefficient of the Large Pressure Surface Half Axis a	–
μ	Coefficient of Friction	–

Symbol	Description	Unit
ν_{Hertz}	Hertz's Coefficient of the Small Pressure Surface Half Axis b	–
ν_{air}	Kinematic Viscosity of the Air	m^2/s
ν	Kinematic Viscosity of the lubricant at operation conditions	mm^2/s
ω_A	Angular Velocity of the Outer Ring	s^{-1}
ω_B	Drilling Angular Speed of the Rolling Element	s^{-1}
ω_I	Angular Velocity of the Inner Ring	s^{-1}
ω_w	Angular Velocity of the Rolling Element	s^{-1}
ω	Angular Speed of the Shaft	rad/s
ρ_{max}	Maximum Pressure	N/m^2
σ	Material Roughness	m

CONTENTS

1 INTRODUCTION

Since the primordial of humanity, production has been conditioned to the speed and mastery of human hands, but everything has changed with the invention of steam machinery during the industrial revolution, making some workers and their machines capable of manufacturing consumer goods in larger quantities and faster than the craftsmen of the time. From that moment on, it was always sought to increase production and decrease its costs, making more people capable of consuming essential goods for their well being. Nowadays, in addition to the quantity and speed of production, the quality of the final product is widely desired. This quality depends on the accuracy and precision of the tools associated with the production process.

Ball screw drives are the most widely used linear actuators in modern machine tools due to their high efficiency and position accuracy (BRECHER et al., 2018). To assure these characteristics a good understanding of the components behavior in working conditions is desired. Test benches, prototypes and different kinds of tests can be necessary, however, they tend to increase costs and time. Another approach for the scientific understanding and to test the effect of changes in a system is to develop a mathematical model and run it on a computer (MARION; LAWSON, 2020).

In the market a great variety of simulation software is available. But since it is not possible to change all variables and geometrical boundary conditions in a commercial software, for research purpose, an in-house developed simulation software is welcome. In this simulation software it is possible to verify how all the calculations are made, to change every single calculation parameter and deeply study the simulated object.

At the WZL of RWTH Aachen University, a calculation software named MTPlus was developed in Matlab for rolling elements characteristics and structure stiffness calculation. The starting version of the software was created for spindle bearing systems. However, in the version prior to the start of this thesis, the calculation software was improved for ball screw drives.

1.1 GOALS

The main goal of this thesis is to consider the temperature as an operating condition in the MTPlus ball screw drives calculation, following the suggestion of Brecher et al. (2018). As presented by Oyanguren et al. (2018), a method to do this is to separate the thermal model from the mechanical model and solve each one separately. To this end, the following specific objectives were established.

- To verify and validate, through experimental results with a test rig, the thermal model previously developed. The geometry of the system was developed in AN-

SYS, and a MATLAB code was used to solve the heat flow between the geometrical components.

- To create a compatibility layer (mapping) between the thermal and mechanical model coordinates, since each one of them uses different geometrical shapes for the finite elements.
- To interconnect both models in an iterative computational process. In the mechanical model, a temperature field from the thermal model is used as input whereas, in the thermal model, the friction calculated in the mechanical model is used as input. This friction will be used to compute the total heat generated during the whole simulation time span.
- To validate the simulation results against experimental data, aiming to ensure that not only the models are correctly implemented, but also the interconnection between them is sound.

1.2 CORRELATION WITH THE ENGINEERING COURSE

In the control and automation engineering course, concepts of electrical and electronics engineering, mechanical engineering and computer science are taught. This work mainly uses the mechanical and computer science concepts learned in the course.

Being one of the main positioning systems used in machine tools, ball screw drives are studied in the lecture EMC5219, Numerical Control Technology. Mathematical models and their implementation in MATLAB are largely used in the control courses (DAS5120 and DAS5142), where the first approach to control a system is to understand its behavior and represent it through a mathematical model. One of the main lectures regarding the mechanical behavior of the material and structures is ECV5215, Solids Mechanics I. In this lecture, stress and strain in axial loads are studied. Concerning the thermal behavior of materials, in the course EMC5425, Transport Phenomen, fundamental concepts in heat transmission were covered. As for the computer science courses related to this thesis, it can be mentioned DAS5103, Numerical Computation for Control and Automation, in which concepts of computational mathematics were introduced, and DAS5102, Information Structure Fundamentals.

1.3 THE INSTITUTE AND THE RESEARCH INFRASTRUCTURE

This project was developed at the Laboratory for Machine Tools and Production Engineering (WZL) of RWTH Aachen University (in German, *Werkzeugmaschinenlabor*

WZL der RWTH Aachen, Figure 1). It is located in the city of Aachen, North Rhine-Westphalia, Germany, sharing borders with Belgium and Netherlands.

Figure 1 – Werkzeugmaschinenlabor WZL der RWTH Aachen.

Source – Facebook of Werkzeugmaschinenlabor WZL der RWTH Aachen, 2016.

Since the establishment of the institute, founded in 1906 by Prof. Dr. Ing. E.h. Adolf Wallichs, the institute has been demonstrating new concepts and strategies in production technology with the aim to cover the entire field of production technology under one roof (The Future of Production Engineering, WZL in Profile (2019)).

The research carried out at the WZL is characterised by close collaboration between the various disciplines as well as a balanced mix of pure research and applied development. Currently the institute employs more than 850 people in its six research areas, which are manufacturing technology, machine tools, production engineering, gear technology, production metrology and quality management.

The presented final project was carried out in the department of Prof. Dr.-Ing. Christian Brecher – Chair of Machine Tools, sector of Machine Tools, under the supervision of Florian Kneer, M.Sc. RWTH.

2 STATE OF THE ART

This chapter presents a literature review about the relevant knowledge fields applied in this work. The first section introduces the finite element method to solve engineering problems, whereas the second section discusses ball screw drives. Subsequently, the existing modelling for mechanical calculation, thermal calculation and the coupling of the models are addressed.

2.1 FINITE ELEMENT METHOD

The finite element method (FEM), also known as finite element analysis (FEA), allows for the numerical solution of field problems. Mathematically, a field problem is described by differential equations (COOK et al., 2001). In this context, FEM is used to numerically solve partial differential equations in complex domains, where the approach is to divide a complex domain into a set of finite simpler sub-domains (HUTTON, 2003). An unsophisticated description of the FEM is that it involves cutting a structure into several elements (pieces of structure), describing the behavior of each element in a simple way, then reconnecting elements at nodes as if nodes were pins or drops of glue that hold elements together (RAHMAN et al., 2008). The arrangement of the elements is called a mesh. A simple mesh can be visualized in Figure 2.

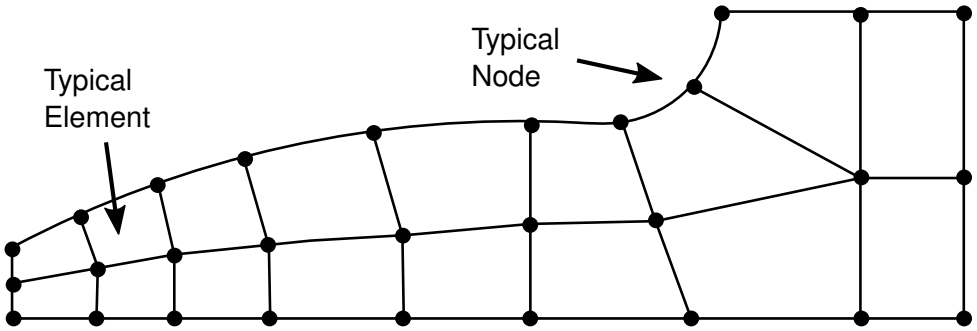

Figure 2 – Finite element mesh.

Source – Adapted from Rahman et al. (2008).

Different structures can be approximated by different elements, each one with their own advantage over the others. The most used elements in the FEM are bars, beams, plates and solid elements. In the sequel, beam and solid elements will be presented.

2.1.1 Beam Elements

A beam element is one of the most capable and versatile elements in the finite element library. It is very commonly used in the aerospace stress analysis industry and

also in many other industries such as marine, automotive, civil engineering structures etc. (BATCHU, 2020). As its name suggests, it consists of a straight line segment with nodes at each end (COOK et al., 2001) and is presented in Figure 3a.

A maximum of three translational degrees of freedom and three rotational degrees of freedom are defined for beam elements. Three orthogonal forces (one axial and two shear) and three orthogonal moments (one torsion and two bending) are calculated at each end of each element (AUTODESK, 2020a). Beam elements are recommended when the length of the analyzed object is much greater than the width and it must handle loads (AUTODESK, 2020a).

2.1.2 Solid Elements

In the FEM, when dealing with complex problems, a volume mesh is necessary. This mesh can be seen as a compound of solid elements such as tetrahedrons and hexahedrons (ALBERICH-BAYARRI et al., 2007). For the purpose of this thesis, only the tetrahedron elements will be discussed. These are solid volumes with four vertices with one triangular face opposite to each one of the four vertices, as shown in Figure 3b.

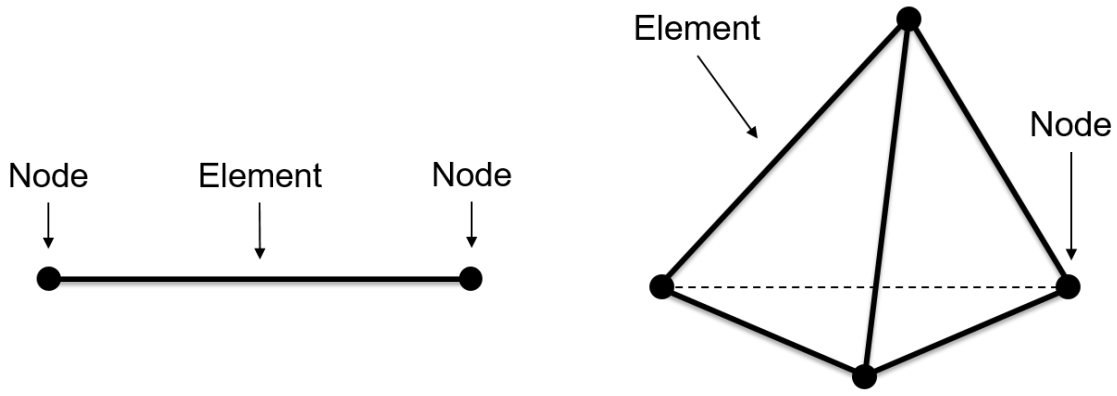

(a) Single Beam Element. (b) Tetrahedron Element.

Figure 3 – Elements in the FEM

Source – Original.

Each node in the tetrahedron has three translational degrees of freedom, in the X, Y and Z directions (AUTODESK, 2020b). As shown in AutoDesk (2020b), thermal gradients defined by the temperature at the nodes may be applied. Thus, with tetrahedrons it is possible to solve heat flux problems.

2.2 BALL SCREW DRIVES

As discussed by Altintas et al. (2011), ball screw drives are one of the most widely used position actuators in machine tools. They are characterized by a high efficiency and thus have low heating, low wear, high service life and a high positioning accuracy (BRECHER et al., 2018).

A ball screw consists of a shaft, supported by bearings at the two ends, a nut system and rolling elements. Both shaft and nuts have raceways, also called grooves, wherein the rolling elements are placed, separating the screw from the nut system (BRECHER et al., 2018). According to Altintas et al. (2011) "One end of the ball-screw is either attached to a rotary motor directly or through gear/belt speed reduction mechanisms". The raceways of the components in the ball screw drive have a helical form. Therefore, a rotational motion in the screw generates a linear motion in the nut, i.e. the ball screw drive converts rotational into linear motion.

To avoid the balls to fall out of the end of the nut, a recirculation mechanism is used. In Figure 4, the external and internal recirculation system are shown.

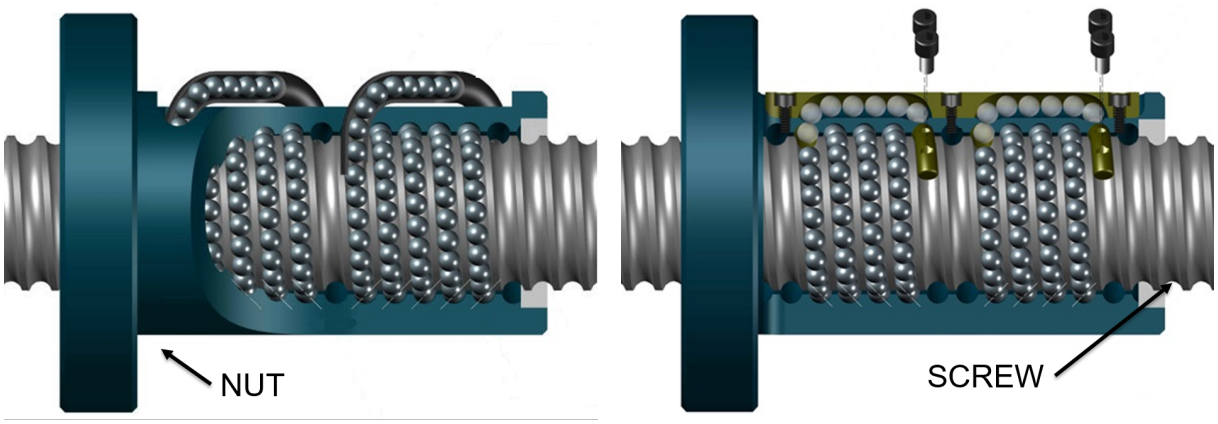

(a) External recirculation system. (b) Internal recirculation system.

Figure 4 – Recirculation Systems.

Source – Adapted from Barnes Industries (2020).

In the external recirculation approach (Figure 4a), the ball is returned to the opposite end of the circuit through a ball return tube or canal, which protrudes above the outside diameter of the ball nut. Alternatively, in the internal recirculation system (Figure 4b) the ball is returned through or along the nut wall, below the outside diameter (BARNES INDUSTRIES, 2020).

2.2.1 Preload and Stiffness of Ball Screw Drives

Preload can be described as a tension induced on the ball screw, creating elastic deformation in the components, by providing an axial load. The purpose of the preload is to prevent loss of ball contact (also know as backlash) and ensure the rigidity of the

component during operation (VERL; FREY, 2010). Thus, preload will result in a higher position accuracy on the driver and in a better quality of the final piece produced by the machine tool. Differents ways to induce preload on the ball screw system are shown in Figure 5.

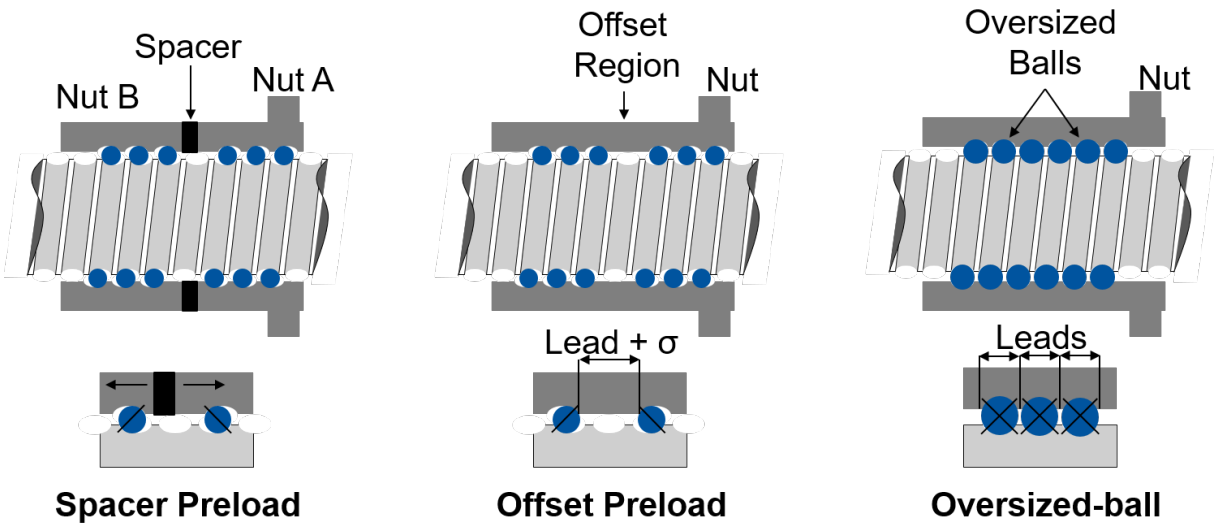

Figure 5 – Ball-screw and nut mechanism.

Source – Adapted from Altintas et al. (2011).

On the *Spacer Preload* a spacer is used to generate the preload on the system by creating a tension between the nut and counter nut, on the *Offset Preload* the preload is provided by increasing the length of one of the leads located in the middle of two ball recirculation circuits and on the *Oversized-ball* the preload is caused by the assembling of larger rolling elements (NSK, 2011).

For the case that the preload is generated by the *Spacer Preload* or by the *Offset Preload* the contact between the balls and the raceway grooves will have two points, whereas the *Oversized-ball* preloading system will have four points of contact.

2.2.2 Contact characteristics

As presented above, the contacts between the ball and the raceway grooves can occur at two or four points. For the aim of this thesis only the two contact points will be explored.

In Figure 6a is shown the preload force F_{ao} induced by the spacer and in Figure 6b the normal force F_N and the angle α of the contact between the ball and the raceway grooves. By means of both figures it is possible to explain how the preload applied in the system will affect the contact characteristics. In Figure 6a an increase of the spacer size in the system will lead to an increase of the F_{ao}. This F_{ao} will result in an increase of the displacement δ between the nut groove and spindle groove in Figure 6b.

Thus, a higher δ will result in an increase of the F_N and the α. The opposite is true, with the decrease of the spaces size, F_{ao}, consequently δ, F_N and α, will decrease.

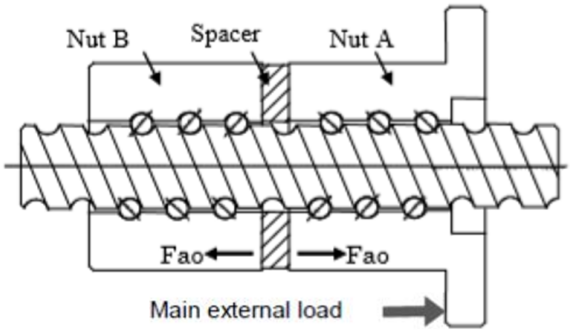

(a) Spacer Preload Nut and ball contact.
Source - (NSK, 2011).

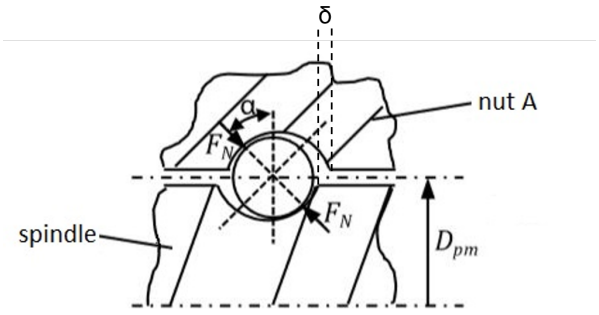

(b) Normal contact forces and contact angle.
Source - Adapted from Brecher et al. (2018).

Figure 6 – Contact Behavior due to the Preload.

As featured by Steinert (1995), elastic bodies are characterised by the fact that they deform under the action of external forces (Figure 7a). Thus, due to the normal contact forces acting on the balls, the contact of the ball with the nut and ball with the spindle will not occur at a single point, but rather through an ellipse with radii *a* and *b*, as displayed in Figure 7b.

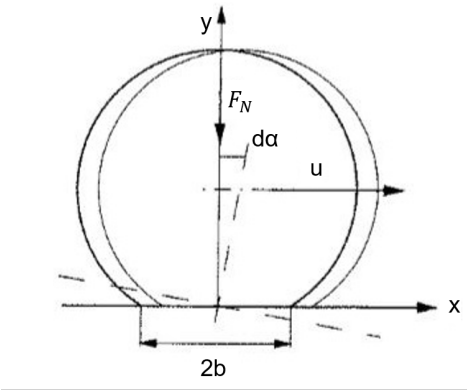

(a) Ball deformation.

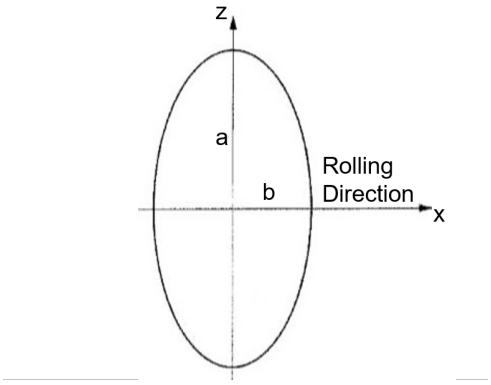

(b) Contact ellipse.

Figure 7 – Ball deformation due to the Normal contact Force.

Source – Adapted from Steinert (1995).

Due to the hysteresis caused by the internal material damping, the elastic potential energy is not reversibly converted back into kinetic energy on the discharge side when the load is released. Instead, a small part of this energy dissipates and heats the ball, nut and spindle (STEINERT, 1995).

2.3 BALL-SCREW MECHANICAL MODELING

The ball-screw mechanical model to be presented in the sequel is the one used in the MTPlus. First, the MTPlus general calculation method will be discussed. Afterwards, friction models existing in the literature will be addressed. These friction models are necessary for the coupling of the models, since the heat is generated by the friction between the components in the ball-screw drive.

2.3.1 Calculation software MTPlus

The final result from MTPlus are the contact characteristics of the rolling elements. These characteristics are dependent on the load distributions, being determined by the elastic deformation of the nuts and the spindle due to the contact forces. However, the elastic deformation and the contact characteristics are interconnected. The MTPlus uses a co-modeling approach to solve this problem. The elastic deformation is determined by a FEA that uses beam elements to approximate the stiffness, mass and damping characteristics of the nuts and the spindle, whereas the contact characteristics are described by a numerical model based on the method for angular contact ball bearings introduced by Tüllmann (1999).

In the Tüllmann model, the contact forces depend on the position of the rolling elements and the grooves. The displacement δ is determined by solving

$$\sum F = K \cdot \delta \Leftrightarrow \delta = K^{-1} \cdot \sum F\,, \tag{1}$$

where $\sum F$ is the sum of forces acting on the rolling elements and K is the stiffness matrix of the rolling elements.

The co-simulation model to determine the interaction between rolling elements and the elastic deformation of the components is presented in Figure 8.

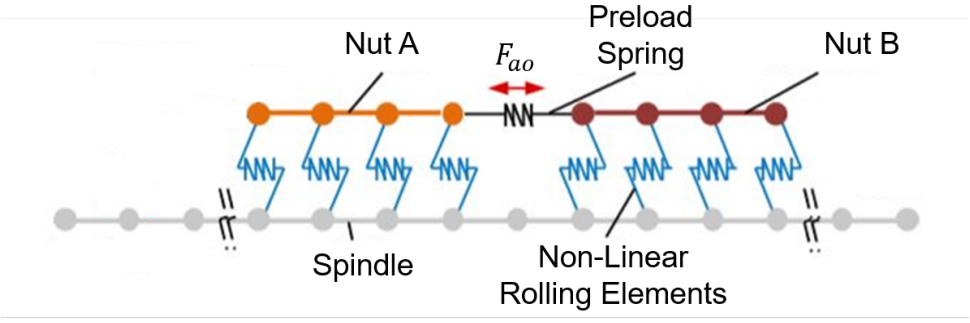

Figure 8 – MTPlus Calculation Model.

Source – Adapted from Brecher et al. (2018).

The model is composed of two parts, geometry components and boundary conditions. The geometry components are the nuts and the spindle and the boundary

conditions are the rolling elements, the preload spring and the fixation to the surroundings. Each boundary is a spring-damper-element connecting two nodes of the geometry components (BRECHER et al., 2018). To be able to simulate the preload forces created by the spacer on the nut system, the spacer is represented by a spring with an extremely high stiffness and the generated preload is a parameter of the spring.

Regarding the software implementation, Figure 9 shows the MTPlus calculation approach.

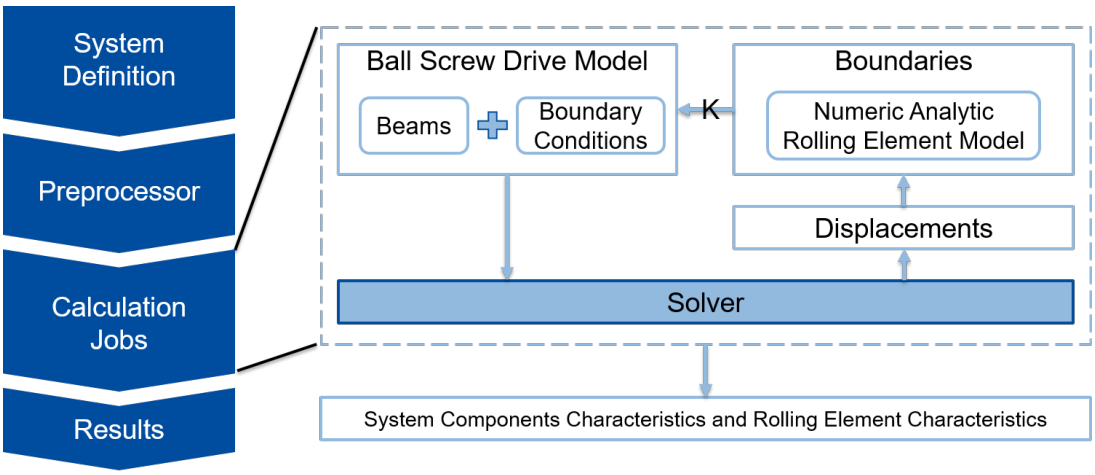

Figure 9 – MTPlus Calculation Approach.

Source – Adapted from Brecher et al. (2018).

In the *System Definition* step the geometry and boundary conditions are defined, such as the temperature of the components, ball diameter, pitch diameter, preload force, i.e., the calculation parameters of the model. Afterwards, in the *Preprocessor*, the system is solved free of load, i.e. the position of the rolling elements are determined and the FEM matrices for the beams are created. At last, different *Calculation Jobs* are executed. In each *Calculation Job* performed, the characteristics of the system components and the rolling elements are computed in an iterative way. The displacement of the balls is used to determine a new stiffness matrix K, that will be used as boundary conditions in the next iteration. When the sum of forces acting on each beam are null, the system calculation stops and the equilibrium is determined.

The *Calculation Jobs* performed on MTPlus are the *Static Equilibrium*, *Static Implicit* and *Static Explicit*, being the last two different approaches for the *External Load* applied on the system. In Figure 10, these calculation are presented.

In each calculation job, different parameters will be introduced in the system. First, on the *Static Equilibrium* job, the preload forces are introduced in the system; After that, speed and thermal functions are executed.

In the *External Load* injection the *Static Equilibrium* results are used as a start point of the calculation. In both approaches, *Static Implicit* and *Static Explicit*, external

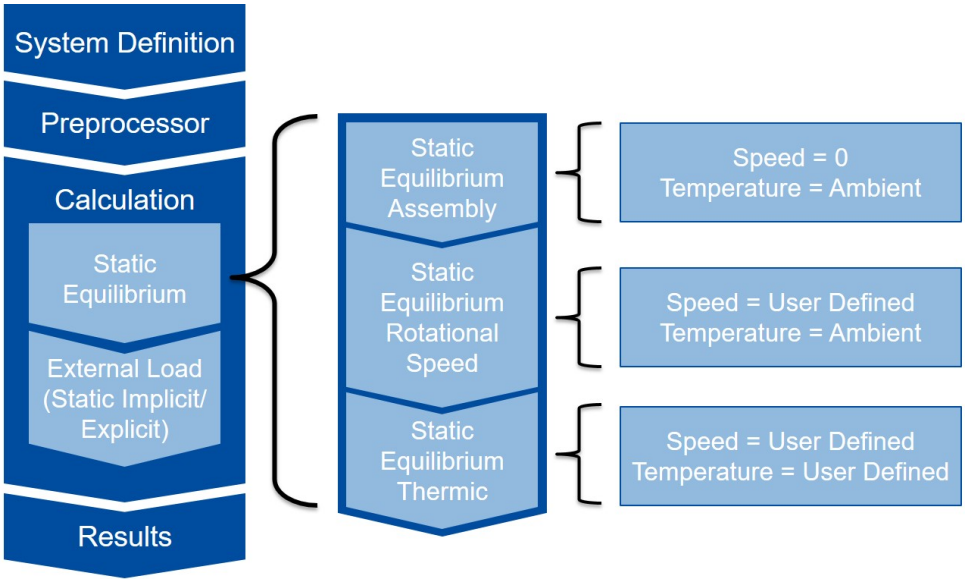

Figure 10 – Static Equilibrium Steps.

Source – Original.

force acting on the system is divided into several partial forces and applied to the system step by step. As discussed by Falker (2020), the difference between the approaches is that on the *Static Explicit* after each step the stiffness of the rolling elements are updated. Otherwise, in the *Static Implicit* not only the stiffness is updated but a new system equilibrium is calculated in an iterative away, which means that a balance between the external forces and the reaction forces on the boundary conditions is determined.

2.3.2 Friction Models

With the aim to calculate the heat generated in the ball-screw interface, the friction forces acting on the rolling elements and in the grooves need to be calculated. In this subsection the models developed by Steinert (1995) and Olaru et al. (2005) will be addressed. The Steinert model is a model developed for ball bearings and it was chosen due to the similarities between the ball bearings and the ball screw. The Olaru Model was developed with the purpose of calculating the friction for the ball screw system.

For the proper understanding of the models it is important to know how the lubrication works and how it affects the kinds of friction existing in the system. Afterwards, the Friction Forces and the Friction Moments acting on the rolling elements for both friction models and their calculations will be displayed.

It is important to address that in some of the literature existing the Elastohydrodynamic (EHD) and the Hydrodynamic lubrication regime are studied separately, but in

the friction models implemented both regimes are compressed as one, although Olaru et al. (2005) present the Hydrodynamic Regime with the EHD acronym.

2.3.2.1 Lubrication

The main idea of lubrication is to reduce friction between surfaces. Assuming two rolling surfaces, such as steel on steel, the roughness of the materials will cause friction. A way to reduce this friction is to have between the surfaces a different material; in this case, a coherent liquid lubricant (GOHAR; RAHNEJAT, 2018).

The Stribeck curve (Figure 11) is a way to represent the coefficient of friction μ to the lubrication parameter λ_S, that relates material roughness σ with lubricant film thickness *h*:

$$\lambda_S = \frac{h}{\sigma}. \tag{2}$$

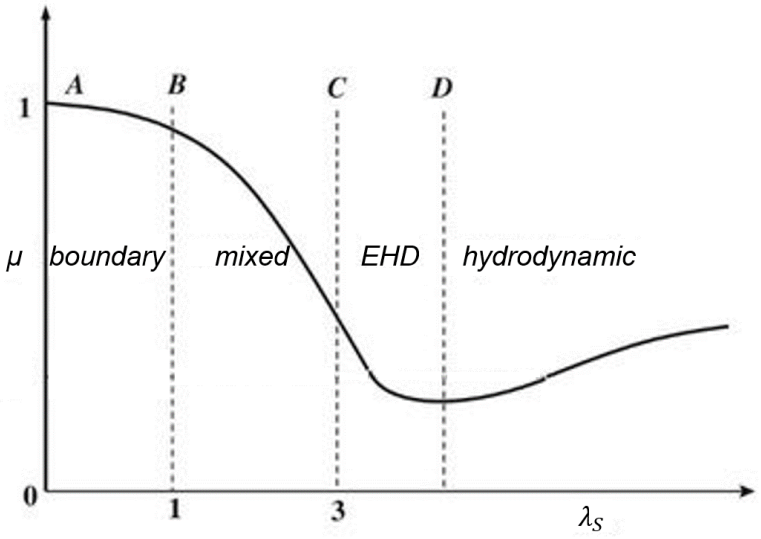

Figure 11 – Friction coefficient due to the parameter λ_S.

Source – (GOHAR; RAHNEJAT, 2018).

According to Gohar and Rahnejat (2018), at the Point *A* the friction contact is a clean surface, which means there is no lubricant film between the surfaces. With the formation of a lubricant film, the system will reach Point *B*, where the surface roughness is equal to the lubricant film thickness. This *AB* regime is called *boundary lubrication*. With the increase of the lubricant film thickness the system will reach points *C* and *D*. In the *BC* regime the load is partly supported by the oil film and partly by a regime-*AB*-type, which is called *mixed lubrication* or *partial lubrication*. At the regime *CD*, called elastohydrodynamic (EHD), the value of λ_S is large enough in such a manner that the lubricant film thickness is not influenced by the surface properties. In this zone

the surfaces distorts elastically and the lubricant viscosity tends to increase. The last regime, beyond *D*, covers the hydrodynamic regime. This zone is reached with the increase of the speed or reduction of the load in the zone *CD*, reducing the elastic distortion of the surfaces. This situation sometimes occurs in ball bearings when some of the rolling elements have become unloaded.

The variable *h* is calculated by Steinert (1995) taking into account the contact ellipse presented in Figure 7b, the speed index *U*, the load index *W*, the material index *G* , the replacement radius of hertzian theory *R*, the Hertz's coefficient of the large pressure surface half axis *a* μ_{Hertz}, and the Hertz's coefficient of the small pressure surface half axis *b* ν_{Hertz}. First, the lubricant film without thermal influence $h_{isotherm}$ is calculated according to

$$\begin{gathered} h_{isotherm} = H_{isotherm} \cdot R \\ H_{isotherm} = 4.3 \cdot U^{0.68} \cdot W^{-0.073} \cdot G^{0.49} \cdot (1 - e^{-1.28 \cdot \frac{\mu_{Hertz}}{\nu_{Hertz}}}) . \end{gathered} \tag{3}$$

Then, the thermal reduction can be applied:

$$h = \Phi_T \cdot h_{isotherm} \tag{4}$$

where the reduction factor Φ_T is dependent on the the thermal load coefficient *L* and its calculation can be found in Steinert (1995). Since the variable *h* is directly correlated to the speed index *U*, it is possible to plot μ against the working speed, as showed in Figure 12.

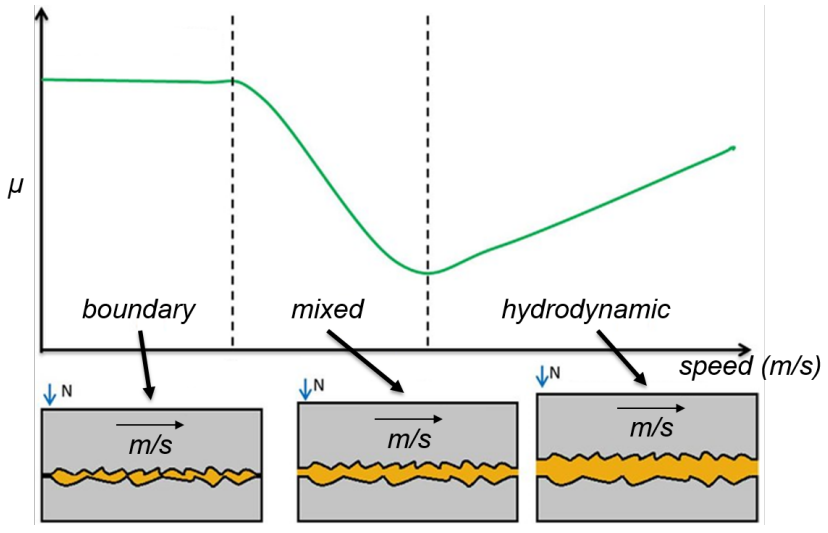

Figure 12 – Friction coefficient due to the working speed.

Source – Adapted from Robinson et al. (2016).

In Figure 12 it is possible to verify that, at lower speeds, no lubricant film is formed between the surfaces. Higher the speed in the system, higher will be the lubricant film thickness present between the surfaces.

Differently from the parameter μ presented by Gohar and Rahnejat (2018), Steinert (1995) defines the relation between the film height and the roughness of the materials as the lubricant film density Λ as

$$\Lambda = \frac{h}{\sqrt{{R_{q1}}^2 + {R_{q2}}^2}}\,, \tag{5}$$

where R_{q1} and R_{q2} are the roughness of the components in contact.

To determine the lubricant regime, a Lubricant Film Factor Λ_{Factor} is defined as

$$\begin{aligned} R_q > 0,1\mu m \quad & \Lambda_{Factor} = 5 \\ 0.1\mu m > R_q > 0.025\mu m \quad & \Lambda_{Factor} = 3 \\ 0.025\mu m > R_q \quad & \Lambda_{Factor} = 2\,. \end{aligned} \tag{6}$$

This factor defines the lubricant regime to be calculated by comparing it to the calculated lubricant film density as

$$\begin{aligned} \Lambda = 0 \quad & \textit{Boundary Regime} \\ 0 < \Lambda \leq \Lambda_{Factor} \quad & \textit{Mixed Regime} \\ \Lambda > \Lambda_{Factor} \quad & \textit{Hydrodynamic Regime}\,. \end{aligned} \tag{7}$$

For the mixed regime, Zhou and Hoeprich (1991) define the calculation model for the friction forces in the system F as

$$F = \lambda \cdot F_{SolidBody} + (1 - \lambda) \cdot F_{Fluid}\,, \tag{8}$$

where the amount of solid body friction $F_{SolidBody}$, i.e. when there is no lubricant in between, and the fluid friction F_{Fluid}, i.e. when the lubricant film is present, are balanced by the percentage factor of each friction λ. This percentage factor is computed as

$$\lambda = e^{-B \cdot {\Lambda_{Factor}}^C}\,, \tag{9}$$

where the parameters B and C are the material and surfaces topology constants.

Differently from the model develop by Steinert (1995), the model proposed by Olaru et al. (2005) uses the relation between the roughness of the components in contact and the lubricant film thickness h to change the value of the friction coefficient used in the friction equations. The friction coefficient value μ_m is calculated as

$$\mu_m = \mu_0 \cdot e^{-B \cdot \Lambda^C}\,, \tag{10}$$

where μ_0 is the friction coefficient parameter due to the contact without lubricant film. The μ_m is calculated respecting the upper and lower boundaries values, being the

upper boundary the calculation parameter μ_0 and the lower boundary a calculation parameter.

The *h* calculation by Olaru et al. (2005) has almost the same inputs as Equation (3) but with different coefficient values in the equation as

$$h = 3.63 \cdot R_x \cdot U^{0.66} \cdot W^{-0.073} \cdot G^{0.49} \cdot (1 - e^{-0.68 \cdot \frac{a}{b}}), \tag{11}$$

where R_x is the equivalent radius in the rolling direction and *a* and *b* are the radii of the contact ellipse in the Hertzian Theory:

$$\frac{a}{b} = \frac{\mu_{Hertz}}{\nu_{Hertz}}, \tag{12}$$

shown by Steinert (1995).

Therefore, the first difference between the models can be seen in the way that the lubricant film thickness will be used in the calculation. In the Steinert Model it defines the percentage of CSB and EHD in the friction components, whereas in the Olaru Model it is a friction coefficient calculation input.

In both models the friction occurs between the rolling element and the inner and outer ring, in Steinert (1995), or nut and screw, in Olaru et al. (2005). All the following calculations will be performed for both contacts, as the calculated results are different for each contact. The calculations for which no explicit distinction is made between the two contacts can be assumed to be equal for both contacts, otherwise, if the calculation is dependent on which contact the friction occurs, the distinction will be shown.

2.3.2.2 Steinert Friction Model

The model developed by Steinert (1995) in *"Das Reibmoment von Kugellagern mit bordgeführtem Käfig"* was developed for ball bearing friction calculation. Due to the similarities between bearings and ball screw, with some adaptations, it is possible to approximate the friction in the system by this model.

The resistance that a ball bearing offers to its rotation is made up of several components, which are:

- Irreversible deformation work on the balls;
- Rolling friction between the bearing rings and the balls;
- Drilling friction between the bearing rings and the balls;
- Sliding friction between the bearing rings and the cage;
- Sliding friction between the balls and the cage.

Since in the ball screw there is no cage the two last components can be disregarded. The rolling friction and drilling friction are both divided between a solid body friction and a fluid friction. Thus, for the ball screw friction calculation based in Steinert (1995), the total friction is made up of three components, to be described in the next subsections.

Irreversible Deformation work on the balls

As already discussed in subsection 2.2.2 and shown in Figure 7, due to the forces acting on the ball and its deformation, the contact area is an ellipse with radii *a* and *b*. This deformation on the ball causes a moment M_A which counteracts the rolling direction:

$$M_A = \frac{3}{16} \cdot \kappa \cdot b \cdot F_N \,, \tag{13}$$

where κ is the damping constant of the rolling element, *b* is the half axes of the contact surfaces and F_N is the normal contact force of the contact points.

The transmission ratio between the rolling elements and the axis of rotation of the bearing or the spindle in the ball screw i_ω is calculated as

$$i_\omega = \left| \frac{\omega_w}{\omega_A + \omega_I} \right| \,, \tag{14}$$

where ω_w is the angular velocity of the rolling element, ω_A the angular velocity of the outer ring and ω_I the angular velocity of the inner ring.

The total frictional torque resulted from irreversible deformation work M_{Aref} on the balls is defined as

$$M_{Aref} = M_A \cdot i_\omega \,. \tag{15}$$

Rolling friction between the bearing rings and the balls

During the rolling process, the ball rotates around its instantaneous pole. Due to the elastic deformation of the ball, the distance between the instantaneous pole and the ball rotations axis is lower than the radius of the ball. Pure rolling can only occur at two points located symmetrically to the y-axis. The distance from the center of contact and the points where the pure rolling happens is designated *d* (Figure 13).

The solid state friction $F_{Coulomb}$ can be defined as

$$F_{Coulomb} = \frac{2}{3} \cdot \frac{\pi \cdot \mu_{Gleit} \cdot b \cdot \rho_{max}}{a^2} \cdot (d^3 - 3 \cdot d \cdot a^2 + a^3) \,, \tag{16}$$

where *a* and *b* are the radii of the contact ellipse (Figure 13), μ_{Gleit} is the Coulomb coefficient of friction for sliding friction, and ρ_{max} is the maximum pressure in the

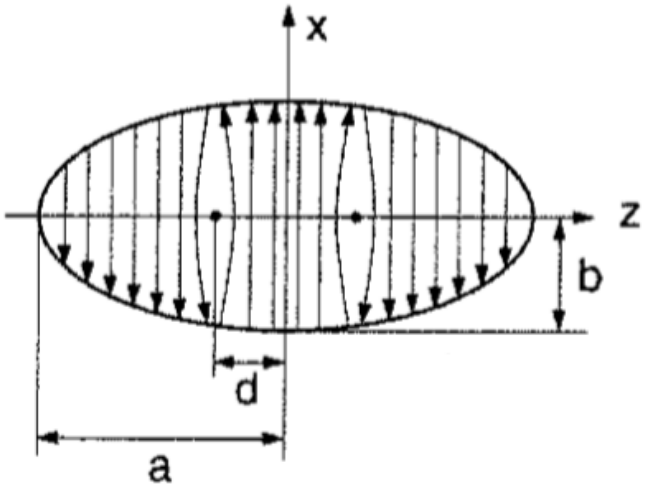

Figure 13 – Print ellipse (displayed strongly magnified).

Source – (STEINERT, 1995).

Hertzian contact surface. The distance d can be calculated iteratively by solving the equation

$$d^5 - \frac{5}{3} \cdot d^3 \cdot (d_\omega^2 + a^2) + 5 \cdot d \cdot d_\omega^2 \cdot a^2 - \frac{5}{3} \cdot d_\omega^2 \cdot a^3 = 0\,, \tag{17}$$

where d_ω is the diameter of the ball.

The fluid frictional force F_{EHD} is computed as

$$F_{EHD} = \mu_{EHD} \cdot F_N\,, \tag{18}$$

where F_N is the contact normal force, and μ_{EHD} is the fluid friction coefficient, defined in analogy to Coulomb's friction theory and according to Gohar (1971). The calculation of μ_{EHD} is performed as

$$\mu_{EHD} = \frac{\Phi_T \cdot 8.6 \cdot \left(\frac{U \cdot G}{W}\right)^{0.8}}{G}\,, \tag{19}$$

where Φ_T is the thermal reduction factor, U is the speed parameter, W the load parameter, and G the material parameter.

After obtaining both solid-state and fluid frictions due to the rolling between the rings and the balls, all the friction forces can be calculated taking Equation (8) and Equation (9). The rolling frictional torque M_B is obtained as

$$M_B = F_B \cdot \frac{d_\omega}{2}\,, \tag{20}$$

where F_B is the the rolling friction force, and d_ω is the ball diameter. Similarly as in Equation (14) and Equation (15), M_{Bref} is calculated as

$$M_{Bref} = M_B \cdot i_\omega \,. \tag{21}$$

Drilling friction between the bearing rings and the balls

Drilling motion appears when the angular velocity vector of the balls is not parallel to the rolling direction. Thereby a rotation of the rolling element perpendicular to the elliptical contact surface exists in addition to the rolling motion. Analogous to the rolling friction, the drilling friction is composed of a solid-body friction component and a fluid friction component. The calculation of the solid-body component in the drilling friction torque $M_{Coulomb}$ is performed as

$$M_{Coulomb} = \frac{1}{8} \cdot \pi^2 \cdot \mu_{Coulomb} \cdot \rho_{max} \cdot (b \cdot \mu_{Hertz})^3 \,, \tag{22}$$

where $\mu_{Coulomb}$ is the Coulomb friction coefficient and μ_{Hertz} is the Hertzian coefficient of the large pressure surface, in this case, as showed in Figure 13, the half-axis *a*.

Regarding the moment due to fluid friction component in the drilling friction torque M_{EHD} the calculation is presented as

$$M_{EHD} = 4 \cdot \frac{\omega_B}{h} \cdot \int_0^b \int_0^{a \cdot \sqrt{1-\left(\frac{x}{b}\right)^2}} \eta(\nu, \rho) \cdot \left(x^2 + z^2\right) \cdot dz \cdot dx \,, \tag{23}$$

where the integration of the viscosity function of the temperature and pressure $\eta(\nu, \rho)$ is made over the ellipse with radii *a* and *b* displayed in Figure 13. ω_B is the drilling angular speed and *h* is the lubricant film height. With the two moment components of the drilling friction in hands, the total drilling friction torque M_C is calculated with Equation (8) and Equation (9).

Analogous to the Equation (14) and Equation (15), the transmission ratio of drilling speed and bearing speed i_B is defined as

$$i_B = \left| \frac{\omega_B}{\omega_A + \omega_I} \right| \tag{24}$$

and M_{Cref} as

$$M_{Cref} = M_C \cdot i_B \,. \tag{25}$$

2.3.2.3 Olaru Friction Model

The model presented by Olaru et al. (2005) in the paper *"A New Model to Estimate Friction Torque in a Ball Screw System"* considers the Forces and the Moments

acting on the ball screw rolling elements. These forces and moment are presented in Figure 14.

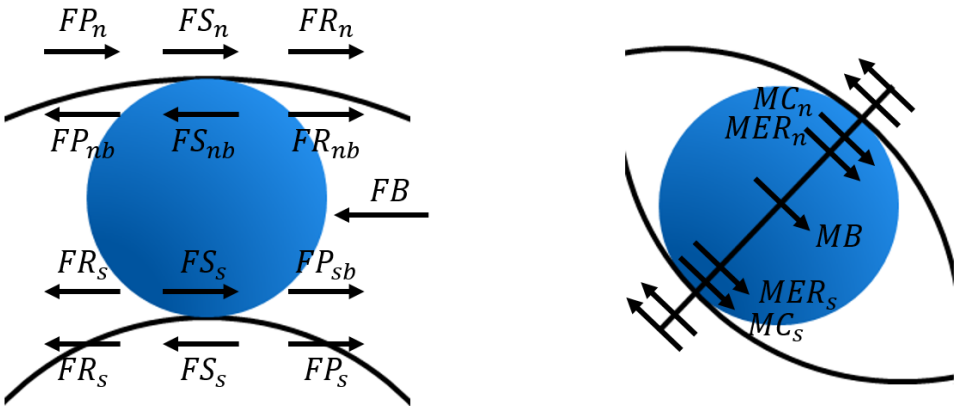

(a) Acting Forces. (b) Acting Moments.

Figure 14 – Olaru Friction Model Components

Source – Adapted from Olaru et al. (2005)

In Figure 14a are shown the hydrodynamic rolling force *FR*, the pressure forces *FP*, the ball to ball forces *FB* and the sliding forces *FS*. The moments are shown in Figure 14b, where *MER* is the elastic resistance in the ball-groove contact, *MC* is the curvature friction moment and *MB* is the moment due to the ball to ball friction.

The factors *n*, *s*, *nb* and *sb* define whether the force acts on the nut, on the screw, on the nut-ball contact or on the screw-ball contact, respectively.

The hydrodynamic rolling force is calculated as

$$FR = 2.86 \cdot E \cdot {R_x}^2 \cdot k^{0.348} \cdot U^{0.66} \cdot W^{0.47} \cdot G^{0.022}, \tag{26}$$

k being the ratio between the radius in the rolling direction R_x and the transversal equivalent radius R_y. The calculation for the R_x, R_y, U, W and G were shown by Olaru et al. (2005).

The sliding forces are calculated "to satisfy the equilibrium of forces and moments" (OLARU et al., 2005), i.e., the sliding force in the system will be counteracting the sum of the others forces and moment components in the calculation. For the sliding force a distinction between the ball-screw and ball-nut contact is made. For the ball-screw the calculation is defined as

$$FS_s = \frac{MC_n + MC_s + MER_n + MER_s + MB}{d_W} + FR_n + \frac{(FR_n + FR_s) \cdot d_W \cdot cos(\alpha)}{d_m} + \frac{FB}{2}, \tag{27}$$

whereas for the ball-nut it is

$$FS_n = \frac{MC_n + MC_s + MER_n + MER_s + MB}{d_W} + FR_s - \frac{(FR_n + FR_s) \cdot d_W \cdot cos(\alpha)}{d_m} - \frac{FB}{2}, \tag{28}$$

where α is the contact angle, d_m is the screw diameter and the d_W is the distance from the base of the groove until the top, its value being close to the radius of the ball.

The computation of the elastic resistance in the ball-groove contact *MER* and the moment due to the ball to ball friction *MB* were demonstrated by Olaru et al. (2005). The calculation of the curvature friction moment is

$$MC = 0.1 \cdot \mu_m \cdot \frac{Q \cdot a^2}{Rd} \cdot (1 - 5 \cdot Y^3 + 3 \cdot Y^5), \tag{29}$$

where Rd is the deformed radius in the ball-groove contact, Q is the contact load, and Y the distance from the center of the contact ellipses to the point of pure rolling. Q is equivalent to F_N and Y is equivalent to the distance d in the Steinert (1995) developed model.

The friction force acting on the rolling element is defined as

$$F = FR + FS, \tag{30}$$

and the friction torque as

$$M = F \cdot R, \tag{31}$$

where R is the radius of the ball-screw contact, at its calculation is different for the ball-screw and the ball-nut contact and can be better studied in Olaru et al. (2005).

2.4 BALL-SCREWS THERMAL MODELING

The aim of the thermal model is to deal with the heat input caused by the components' friction and the heat diffusion on the components of the model. In the sequel will be presented, heat transfer concepts and the existing ball-screw thermal model on the literature.

2.4.1 Heat Input

In the model developed by Oyanguren et al. (2018) the heat in the ball screw system is calculated considering the frictions of the rolling elements on the nut-screw interface and on the bearings that supports the screw. These heat inputs are shown in Figure 15.

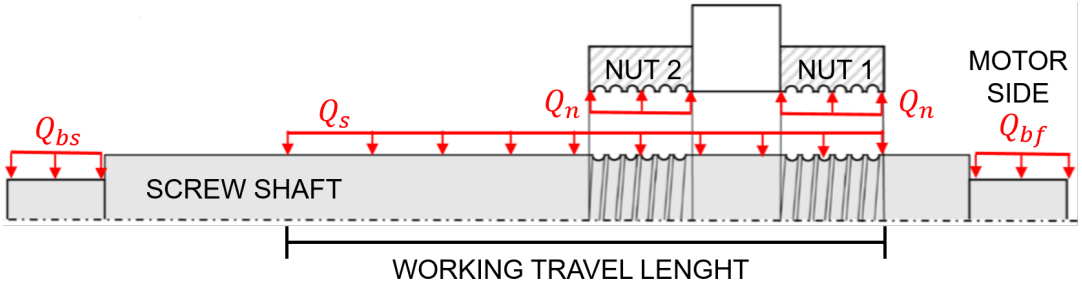

Figure 15 – Thermal Scheme of Heat Generation.

Source – (OYANGUREN et al., 2018).

As presented by Oyanguren et al. (2018),

$$Q_n = \frac{Q_{ns}}{2} \quad \text{and} \quad Q_s = \frac{Q_{ns}}{2}, \tag{32}$$

where heat generation of the rolling elements in the nut-screw interface Q_{ns} is divided equally between the heat fraction acting on the nut Q_n and the heat fraction on the screw shaft Q_s. The total heat generated in the nut-screw interface is the product of the sum of the frictional torque of the ball-screw rolling elements Mr_n and the angular speed ω as

$$Q_{ns} = Mr_n \cdot \omega\,. \tag{33}$$

Since the nut travels along the spindle, Q_s is comprehended in the working travel length of the ball screw, as shown in Figure 15.

Similarly to the heat generated in the nut-screw interface, the heat generation of the bearing on the motor side

$$Q_{bs} = \frac{Mr_{bs}}{2} \cdot \omega\,, \tag{34}$$

and the heat generation of the bearing on the opposite side of the motor

$$Q_{bf} = \frac{Mr_{bf}}{2} \cdot \omega\,, \tag{35}$$

are dependent on friction torque Mr_{bs} and Mr_{bf} of each bearing and the angular speed ω. In the Oyanguren et al. (2018) model the friction torque for the bearings is a parameter of the bearings implemented. The total friction torque calculated for the bearings is divided by two because only half of the heat generated is applied on the spindle.

2.4.2 Heat Diffusion

Heat is the energy that flows from the higher level of temperature to the lower due to an existing temperature gradient. According to Pentenrieder (2005) the equations for

any kind of heat transfer fit into the pattern

$$\text{flow} = \text{transport coefficient} \cdot \text{potential gradient}, \tag{36}$$

where *potential gradient* represents a derivative or difference expression, *flow* is the heat flux $\dot{q}$ or the heat transfer rate $\dot{Q}$ and the *transport coefficient* is directly dependent on the transfer mode. The heat diffusion is characterized by radiation, convection and conduction. Due to the temperatures of the ball screw drives, the radiation can be neglected (OYANGUREN et al., 2018). Thus, in the sequel, the calculations regarding to the conduction and convection between the ball-screw components and between the components and the environment will be presented.

2.4.2.1 Conduction

Conduction is characterized by the transfer of heat between two bodies or from one part of a single body to another part due to the difference of temperature. The conduction process occurs on a molecular level, where the more energetic molecules transfer their energy to the less energetic molecules (ROHSENOW et al., 1998).

The heat flux $\dot{q}$ is calculated as

$$\dot{q} = -\lambda_{heat} \cdot \Delta T, \tag{37}$$

where the heat transfer coefficient of the material λ_{heat} and the temperature difference of the bodies ΔT are taken into account.

On the themal model developed by Oyanguren et al. (2018) conduction will occur on the nut-screw interface as shown in Figure 16 and internally on the components.

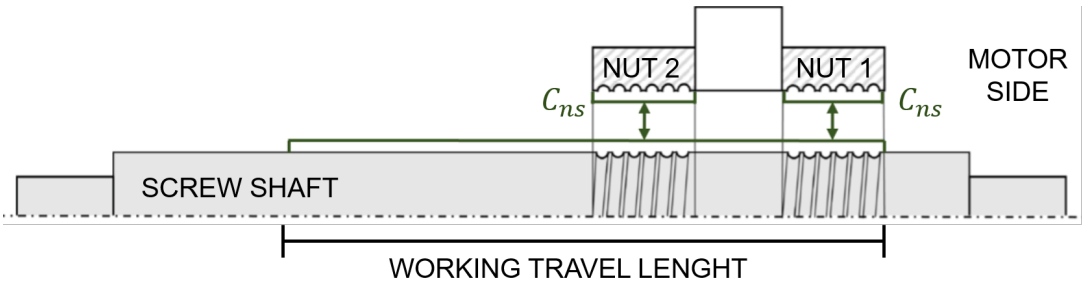

Figure 16 – Thermal Scheme of Conductance.

Source – (OYANGUREN et al., 2018).

2.4.2.2 Convection

Convection relates to the transfer of heat from a surface to a fluid in motion. According to Rohsenow et al. (1998), the motion of the fluid can be separated into *forced*

convection, when a device forces the fluid motion, and *free* or *natural convection*, when the motion occurs as a result of the density difference produced by the temperature difference.

On the thermal model presented by Oyanguren et al. (2018) convection happens on the screw and on the nuts, as shown in Figure 17.

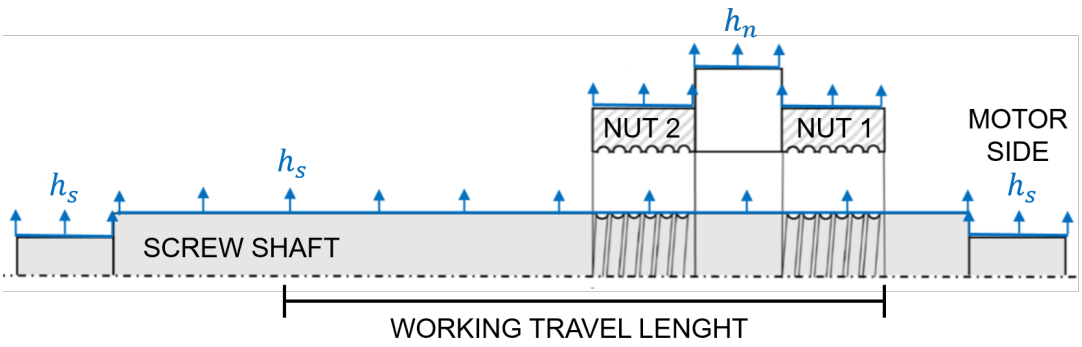

Figure 17 – Thermal Scheme of Convection.

Source – (OYANGUREN et al., 2018).

In Figure 17 the convection action on the screw is referred to as h_s and to the convection on the nuts as h_n.

In the convection, instead of using the λ_{heat}, a coefficient for forced convection h_{forced} and free convection h_{free} is introduced by Oyanguren et al. (2018) and Rohsenow et al. (1998).

Referring to the cases of the forced convection the first parameter to be determined is the Reynolds Number R_e as

$$R_e = \frac{S_{sur} \cdot d_0}{\nu_{air}} . \tag{38}$$

This parameter defines if the air that flows on the external surface is laminar or turbulent (Figure 18) and it is dependent on the speed of the surface S_{sur}, the dimension of the analyses element d_0 and the kinematic viscosity of the air ν_{air}.

If the R_e is lower than a critical value the flow regime will be laminar, otherwise, if it is higher than the critial value, it will be turbulent. The Critical Reynolds Number is dependent on the geometry of the piece where the forced convection occurs and can be studied on VDI-Wärmeatlas (2013) and Rohsenow et al. (1998).

After defining the Reynolds Number, the Nusselt Number in the Forced Convection Nu_{Forced} is computed. This parameter is dependent on the kind of flow regime and the geometry of the component, so for simplification purposes Nu_{Forced} can be defined as

$$Nu_{Forced} = f(R_e, P_r) , \tag{39}$$

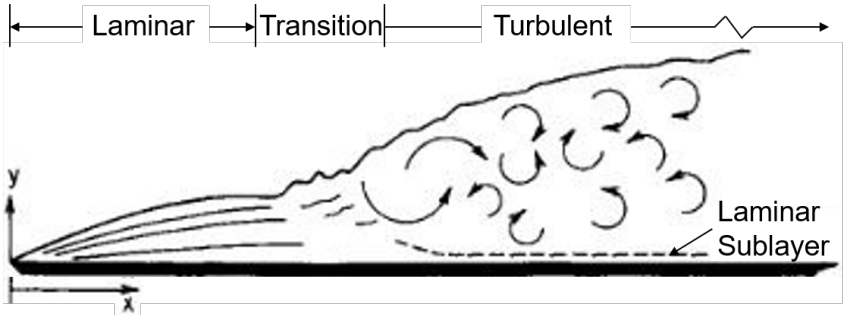

Figure 18 – Laminar, transition, and turbulent boundary layer flow regimes.

Source – Adapted from Rohsenow et al. (1998).

a function of the Reynolds Number and Prandtl Number P_r. The exact Nusselt Number equations were demonstrated for instance by the VDI-Wärmeatlas (2013).

To calculate the h_{forced} the Nusselt Number, the conductivity of the air k_{air} and the dimension of the analysed element are used in

$$h_{forced} = \frac{Nu_{Forced} \cdot k_{air}}{d_0} . \tag{40}$$

The equation for the free convection coefficient is similar to Equation (40), but instead of using the Reynolds Number as a parameter for the Nusselt Number, in the calculation of the Nusselt Number for free convection Nu_{Free} the Rayleigh Number R_a is calculated as

$$R_a = \frac{g \cdot {d_0}^3 \cdot \beta_{air} \cdot \Delta T}{(\nu_{air} \cdot \alpha_{air})} , \tag{41}$$

and it is used as

$$Nu_{Free} = f(R_a) . \tag{42}$$

In Equation (41), g is the gravity, β_{air} is the heat expansion coefficient of the air and α_{air} is the thermal diffusivity of the air.

2.5 THERMO-MECHANICAL COUPLING

Oyanguren et al. (2018) in the paper *"Thermo-mechanical modelling of ball screw preload force variation in different working conditions"* presented two different approaches for the connection of the thermal and mechanical models for ball-screw drivers. On the Non-Updated Heat (NUH) the thermal problem is first fully solved and then the mechanical model is computed by mapping the temperature field. Otherwise, on the Updated Heat UH, the thermal and mechanical model are solved in a loop approach, in this case mechanical variations obtained in the mechanical models are used by the thermal model to change the heat input value.

A temperature mapping to enable the mechanical model to use the temperature distribution obtained from the thermal model and compute the thermal expansion of the components is shown to be necessary. In the Oyanguren et al. (2018) work both models are developed in Abaqus, a commercial software, and the communication between the two models is done using subroutines in Abaqus.

3 EXPERIMENTAL SETUP

In this chapter, the experimental test rig implemented in the previous works and the new implementations performed on this project will be presented. The understanding of the test rig is important since the geometry of both models are based on the test rig assembly. The aim of the test rig is to validate the models results against experimental data.

In the following subsection, the assembly of the test rig, the data acquisition previously implemented and the data acquisition implemented in this project will be discoursed.

3.1 TEST RIG ASSEMBLY

The test rig assembly is presented in the figures in sequence. In the assembly, two ball-screw systems are implemented, one with the aim to measure the displacement on the system and another one to carry the hydraulic actuators that generates an external load in the system. In Figure 19 the nuts, hydraulic actuators and the sensor on the ball-screw system are presented.

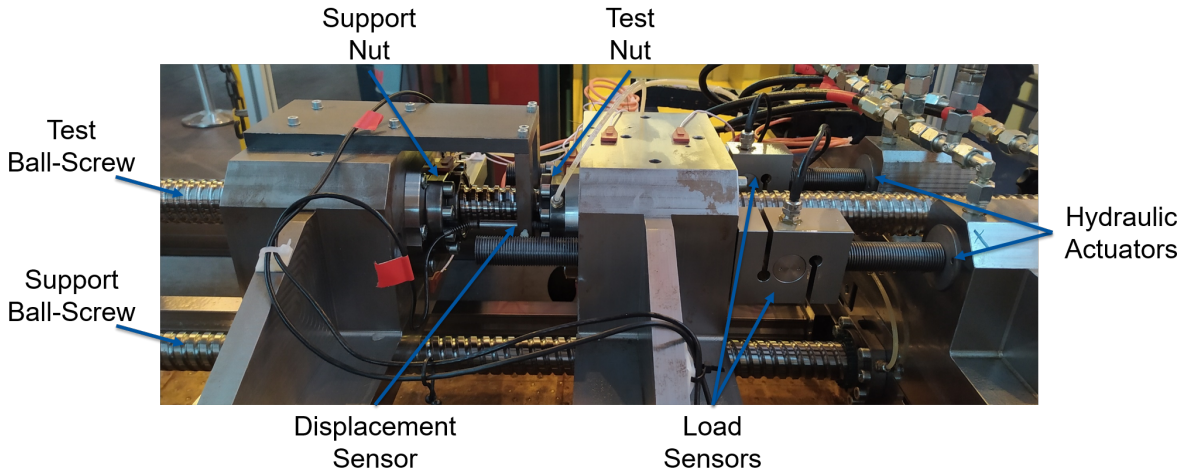

Figure 19 – Test Rig Components.

Source – Original.

Primarily, on the *Test Ball-Screw* two nut systems are implemented. The *Test Nut* is the one where the data will be measured and the load will be applied and the *Support Nut* has the aim to support the *Displacement Sensor* that will measure the relative displacement between the *Test Nut* and the *Spindle* due to the forces acting in the system. On Figure 19 only one *Displacement Sensor* is shown, but in the test rig two are installed, placed on opposite sides parallel to the screw.

The *Support Ball-Screw* is implemented with the aim to move the *Hydraulic Actuators* during the working travel of the nuts in the *Test Ball-Screw*, thus, making it possible to apply the external load on the *Test Nut* during the travel. *Load Sensor* are used to measured the load applied by the *Hydraulic Actuators*.

Both ball-screws in the assembly are supported by bearings on both ends, but for the purpose of this thesis the ones in the *Test Ball-Screw* are presented in Figure 20.

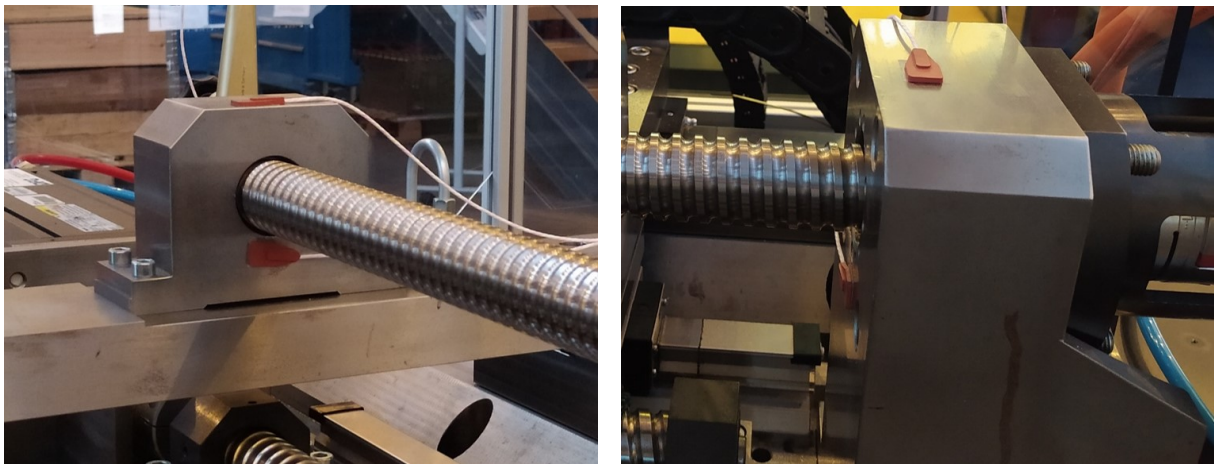

(a) Loose Bearings. (b) Fixed Bearings.

Figure 20 – Support Bearings on the Test Screw.

Source – Original.

The *Fixed Bearing* is the one placed on the motor side. In the assembly two bearings of the model ZKLF3080-2RS-PE are used on the motor side and two bearings of the model 66206-2RSR are used as *Loose Bearings*. Both models presented are produced by Schaeffler Technologies.

Concerning the operation of the test rig a Programmable Logic Controller (PLC) controls the nuts travel by modifying the motor speed and the external load applied using the hydraulic actuator. In the Human-Machine Interface (HMI) it is possible to define the amount of external load applied to the system, the travel length of the nuts, maximum speed, acceleration and the number of pendulum movements.

3.2 DATA ACQUISITION

Previously Implemented

As presented in Figure 19 the data acquisition previously implemented was composed by *Displacement Sensor* and *Load Sensors*.

The *Displacement Sensor* is a Linear Variable Differential Transformer (LVDT) that measures the displacement between the *Test Nut* and the *Spindle*. It is important to mention that before each test the sensor value is set to zero, this way the LVDT data measured is affected only by the thermal delta of the components, the external load

applied by the hydraulic actuators and the motion on the system during the working period.

The *Load Sensors* are located in the connection of the hydraulic actuators and the *Test Nut* to measure the external load applied to the system and enable the PLC to control the amount of external load applied during the tests.

A Data Acquisition System (DAQ) manages the sensors' connection with the computer. For more information regarding the existing data acquisition, the reader is referred to the thesis of Benincá (2019).

New Implementation

With the aim to validate the thermal model implemented the temperatures of the test rig need to be measured. The sensors available are resistance thermometers, more precisely PT100 sensors. Since these sensors have to be directly in contact to the measured body it is not possible to fix it to the bearings, the spindle and some parts of the nut.

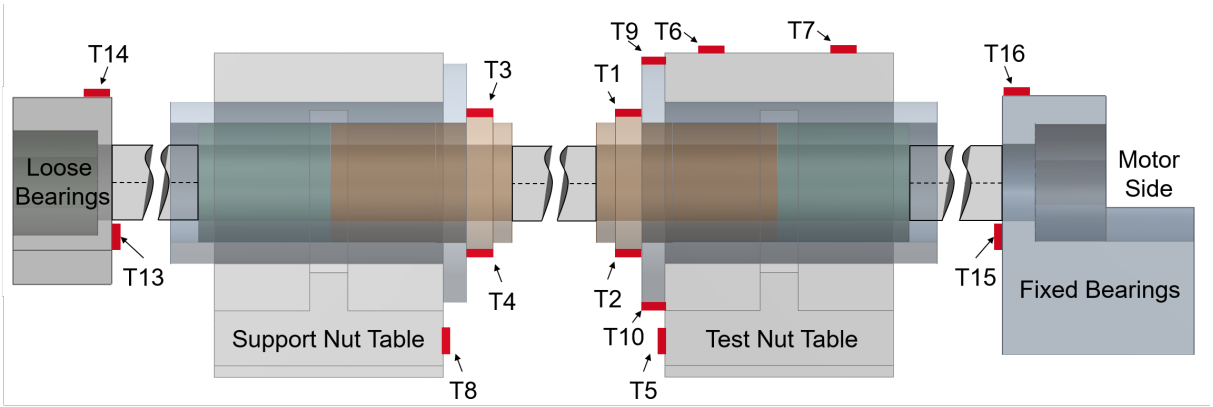

Figure 21 – Thermal Sensors

Source – Original

In Figure 21 is presented the places where the sensors are attached. There are two sensors in the fixed bearing support (*T15* and *T16*) and two in the loose bearing support (*T13* and *T14*) to measure the heat generated by the bearings and the heat flow in these components.

Regarding the components affected by the heat generated by the nuts, there are three sensors on the test nut table (*T5*, *T6* and *T7*), two in the test nut socket (*T9* and *T10*), one in the support nut table (*T8*), two on the outer part of the test nut (*T1* and *T2*) and two on the outer part of the support nut (*T3* and *T4*). These sensors will measure the amount of heat generated by the nut-screw interface and the temperature difference of the components in contact. Thus, making it possible to validate not only the heat generation on the model, but also the heat diffusion on the system.

To measure the environmental temperature, two sensors were placed in different metal pieces, each one located on one side of the test rig.

The thermal sensors are connected to the Data Acquisition System in the same way as the other sensors. Thus, the DAQ was facilitated by the fact that a LabVIEW software was already implemented, this way the only necessity was to add the thermal sensors in the existing program. The user interface on LabVIEW was changed to show the sensors' temperature during the running time. The frequency of the data acquisition on the PT100 was set as 1 Hertz due to the fact that the temperature of the test rig components does not change rapidly.

By the fact that the PT100 are not attached to the moving parts, a few tests were performed using a thermal camera to measure the spindle temperature during the working time. The thermal camera available is a FLIR E50, this model has an accuracy of ± 2 ℃. Due to the fact that the spindle is rotating during the test, and the surface of it is not perfectly cylindrical due to the threads existing, the sensor values are not accurate. Thus, the thermal camera was only used to investigate the shape of the slope of the temperature over the time, not the values at steady state.

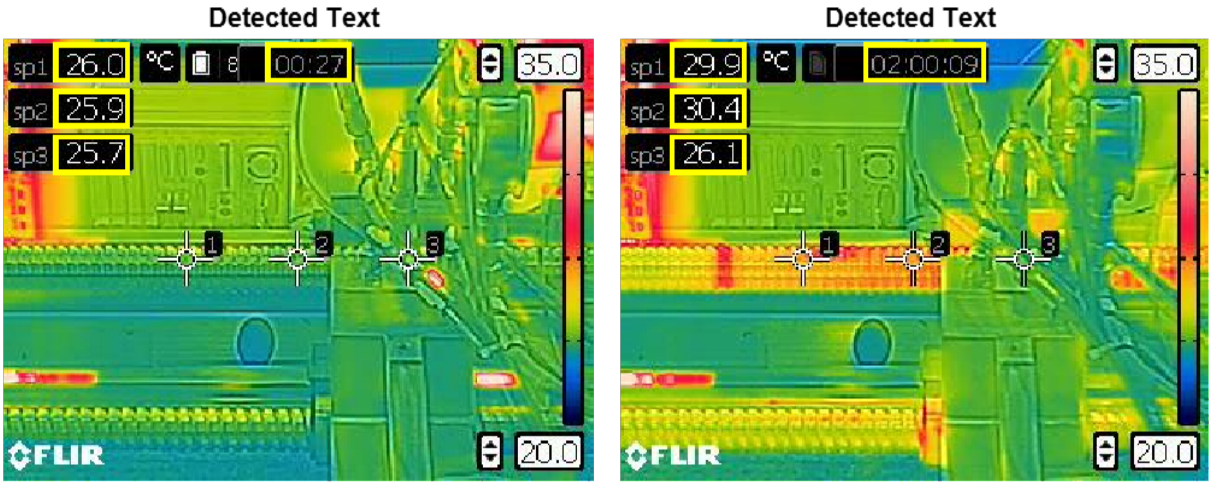

(a) Start of the Test. (b) End of the Test.

Figure 22 – Thermal Camera Frames.

Source – Original.

The measurements were performed in the spindle area that is in contact with the nut. Thus, during the test, sometimes the measurement will be performed in the other components of the nut system and not in the spindle. To extract the right data the first step was to get only specific frames from the video where no component was covering the spindle and the measurement is as clean as possible.

With the right frames the values were extracted from it using the Optical Character Recognition function available in the Computer Vision Toolbox of the MATLAB (Figure 22). At last, as shown in Figure 23, the data from the thermal camera was

interpolated to have the same frequency as the PT100 data and filtered to remove the existing noise.

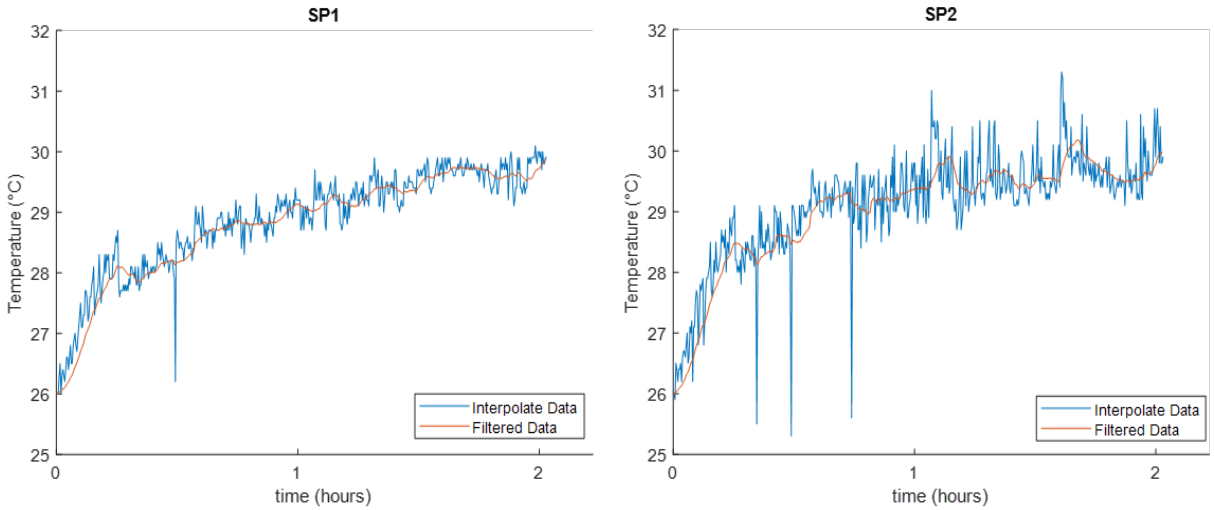

(a) Point of Measurement SP1.

(b) Point of Measurement SP2.

Figure 23 – Thermal Camera Extract Data.

Source – Original.

On Figure 23 the *Interpolated Data* have a great amount of noise in the signal due to the inaccurate measurement from the thermal camera. The *Filtered Data* has the aim to remove the noise, in the Low-Pass Filter implemented a choice is make necessary, if the cutoff frequency on the filter is too low, the noise will be better removed but the first order characteristic of the measured signal will be lost. By contrast, if the cutoff frequency is raised, the first order characteristic will be maintained but the noise present in the filtered data will be higher.

Before comparing the experimental data with the thermal model results, a post processing is performed. First, the mean of the thermal sensors *T11* and *T12* at the starting time is taken as an environmental temperature. For each sensor data a thermal delta between the first measurement and the initial environmental temperature is calculated. After that, this delta is subtracted from the data set of this sensor. Thus, all the sensors' data were set to start at the same value. This assumption is only valid because between different tests a long cooling time is given, so it was possible to assume that all components start at the same temperature.

4 THERMAL MODEL MODIFICATION

The thermal model available in the beginning of this final project work was in development. The geometry, the thermal connection between the components and the heat losses from the components to the environment by convection were implemented.

The geometry was developed on ANSYS, a commercial software, and it is divided in components that belong to three different assembly groups and are presented in Figure 24 and Figure 25

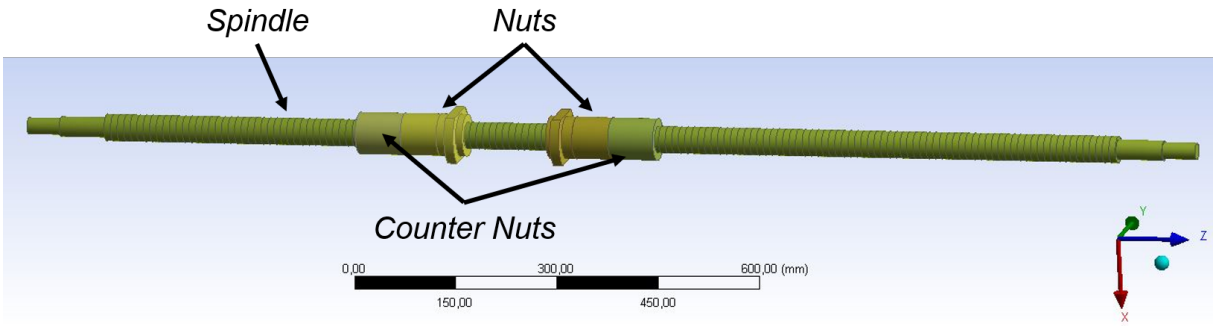

Figure 24 – Components at Assembly Groups *BG1* and *BG2*.

Source – Original.

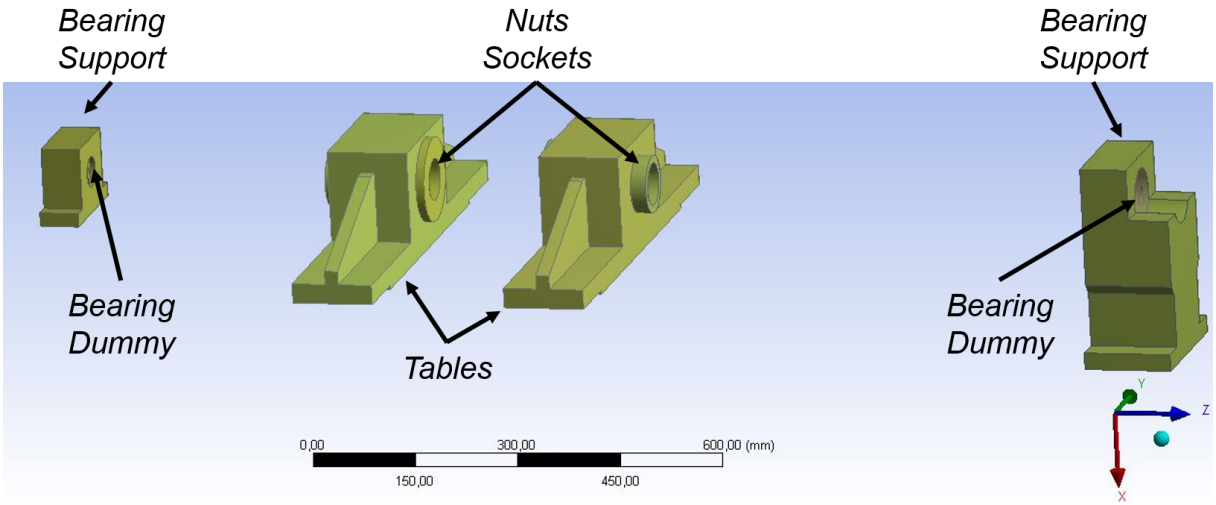

Figure 25 – Components at Assembly Group *BG3*.

Source – Original.

The shaft belongs to *BG1*, the nuts and counter nuts to *BG2* and the bearing supports, tables, nuts sockets and bearing dummies to *BG3*. When the heat flows between the nodes that belong to the same component it is fully computed by the Finite Element Matrices. Otherwise, when the heat flows between different components a

calculation in Matlab functions is performed. The surfaces of the components in contact are called PIN and its temperature is the mean of the nodes that compose the surface and the heat is calculated between these surfaces and not between each node.

At each iteration step in the thermal model algorithmic the heat flux between the PINs is calculated and afterwards the Finite Element Matrices are solved. The Finite Element Matrices are calculated for each assembly group. The calculation is made as following:

$$\begin{aligned} Q_{rr} &= MB + dt \cdot A \\ q_r &= MB \cdot T_r + dt \cdot B \cdot u \\ T_r &= Q_{rr}^{-1} \cdot q_r \,, \end{aligned} \tag{43}$$

where **MB** is the mass information matrix that contains the heat capacity of each node, **A** is the pure stiffness matrix that contains the thermal conductance of the nodes, d_t is the temporal increment of each iteration, $\mathbf{T_r}$ is the column matrix of the nodes temperature, **B** is the area matrix that relates the PIN to the nodes that compose it and **u** is the heat flux column matrix calculated by the Matlab functions.

The systemic representation of the thermal model is demonstrated in the Figure 26.

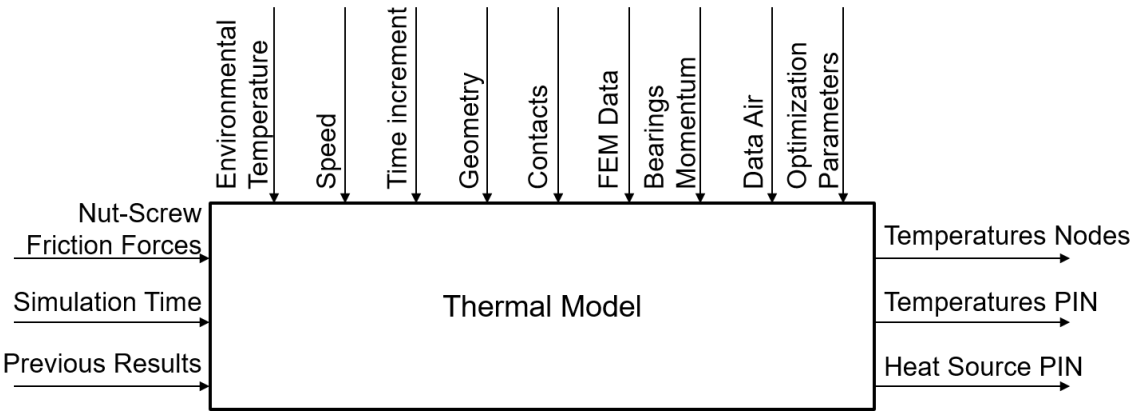

Figure 26 – Thermal model inputs, parameters and outputs.

Source – Original.

With respect to the inputs of the model, the *Nut-Screw Friction Forces* will be the sum of the frictions acting in each rolling element of the nut-screw interface , the *Simulation Time* is how many seconds should be simulated by the thermal model and the *Previous Results* are the temperature from the previous Thermal Model Simulation and it will used in the connection between the models if the *Updated Heat* calculation approach is chosen.

The parameter *Environmental Temperature* is set by the user before each simulation being performed, during all the simulation performed in this work it was chosen the initial temperatures from the postprocessed data from test rig that the model will be compared. The *Time Increment* defines how many seconds will be computed in each simulation step. The parameters from the ANSYS geometry developed are the *Geometry*, *Contacts* and *FEM Data*, that includes the Finite Elements Matrices. The *Bearings Momentum* includes the parameters of the bearings models in the assembly presented in chapter 3. The *Data Air* contains the specific heat, kinematic viscosity, Prandtl number and other air parameters for different temperatures in ℃. The *Optimization Parameters* are defined with the optimization of the model, it will be explained in the final subsection of this chapter.

The outputs of the thermal model are the *Temperature Nodes*, the *Temperature PIN* and the *Heat Source PIN*. These are matrices that store the data for each thermal model iteration. On the *Temperature PIN* are stored the mean value of the nodes that compose the PIN and on the *Heat Source PIN* are stored the heat flux of each PIN.

In this final project work the heat flux calculation in the PINs was revised and improved and new parameters of the calculation were defined in the model to perform the optimization. The Finite Element Matrices and the geometry were only studied to understand the behavior of the model, but none was revised or changed.

Next it will be presented the new implementations on the thermal model. First, the heat flux implementation will be addressed. Afterwards, the solutions related to the heat input in the system are displayed. At last, the new parameters inserted in the model and their optimization as a solution to reduce the error between the model and the experimental setup are shown.

4.1 HEAT FLUX

Regarding the PIN to PIN heat exchange it is important to understand how it is defined in the algorithm. The surfaces in direct contact are called *CONTACT*, that is the one nearby the rotation axis of the spindle, and *TARGET*, the one far from the rotation axis of the spindle. The *CONTACT* temperature is called T_{ACTIVE} and the *TARGET* temperature is called $T_{PASSIVE}$. In the previous functions the heat flows from the T_{ACTIVE} to the $T_{PASSIVE}$, in this case it was possible for the heat to flow from the lower temperature to the higher temperature. Thus, the first implementation made in the thermal model was to redefine the heat flux between PINs.

For the *CONTACT* PIN the calculation is defined as:

$$u = -\alpha \cdot (T_{ACTIVE} - T_{PASSIVE}), \tag{44}$$

and for the *PASSIVE* PIN as:

$$u = \alpha \cdot (T_{ACTIVE} - T_{PASSIVE}), \tag{45}$$

where α is the heat transfer coefficient. With these calculations defined the heat flows from the higher temperature component to the lower.

The value of the α for the multiples contacts existing in the model is based on the literature, regarding to the fact that divergences in the literature exist. As an example Oyanguren et al. (2018) defines the α for the thermal flux between the nut and the spindle as 300 W/m^{2}K concerning the fact that experimental measurements performed by Fletcher and Ford (2003) result in a value of 66 W/m^{2}K. Thus, in the thermal model developed in this work the heat conductance will be defined in the optimization process explained in the end of this chapter.

In the calculation of the heat losses by the PINs to the environment multiple functions were implement based on VDI-Wärmeatlas (2013). In the bearings supports and bearings dummies just free convection was implemented by the fact that there is no motion. Apart from that, the supports of the nuts, the sockets, the nuts and the spindle during the simulation time can or cannot have motion on it, this way, forced and free convection functions need to be implemented. Since the geometry of the component influences the heat transfer coefficient calculation the implemented functions are presented in Table 1.

Assembly Group	Motion	No motion
BG1	Dynamic Free Cylinder Dynamic Plane Lengthwise	Static Horizontal Cylinder Static Vertical Plane
BG2	Dynamic Free Cylinder Dynamic Plane Lengthwise	Static Horizontal Gap Static Horizontal Cylinder Static Vertical Plane Static Horizontal Plane 1
BG3	Dynamic Free Cylinder Dynamic Plane Lengthwise	Static Horizontal Gap Static Horizontal Cylinder Static Vertical Plane Static Horizontal Plane 1 Static Horizontal Plane 2 Static Horizontal Cylinder In Static Inclined Plane

Table 1 – Convection Functions

Source – Original

Between the socket and the nut and between the socket and counter nut a gap exists. Performing the calculation as presented in VDI-Wärmeatlas (2013) for Horizontal Gap the condition for Rayleigh Number is not satisfied by the fact that the gap between the components is too small. As shown by Gobin and Perot (1999), in some cases when the Rayleigh Number is lower than a critical value, no convection happens in the fluid and the heat flows by conduction using the fluid as a mean. Therefore, the function for this gap calculation takes this into account.

4.2 HEAT INPUT

In the thermal model three different heat sources are defined, being the loose bearing, the fixed bearing and the nut-screw interface.

4.2.1 Bearings Heat Input

With respect to the bearings, first the friction for each bearing model needs to be calculated. These calculations are dependent on the bearings model in the test rig assembly. In the Wälzlager Katalog (2014) the calculation friction torque M_{rs} for the bearings model on the loose side is calculated as

$$M_{rs} = M_0 + M_1 \,, \tag{46}$$

where speed dependent friction torque M_0 and a load dependent friction torque M_1 need to be calculated. In this project the load dependent friction torque is disregarded by the fact that the loose bearing is not on the flux of the forces acting in the system.

For the speed dependent friction torque there are two different calculations, one in the case that the kinematic viscosity of the lubrication at operating temperature ν times the operation speed n is equal or higher than 2000 $mm^2min^{-1}s^{-1}$

$$M_0 = f_0 \cdot (\nu \cdot n)^{2/3} \cdot {d_M}^2 \cdot 10^{-7} \tag{47}$$

and other where it is lower than 2000 $mm^2min^{-1}s^{-1}$

$$M_0 = f_0 \cdot 160 \cdot {d_M}^2 \cdot 10^{-7} \,. \tag{48}$$

In Equation (47) and Equation (48), f_0 is the bearing coefficient for speed dependent friction torque and d_M is the medium bearing diameter. f_0 and d_M are bearing parameters from Wälzlager Katalog (2014), for the bearing model 62206-2RSR. For the case of the fixed bearing model assembled in the test rig, the friction torque used is the reference value found in Wälzlager Katalog (2014), it being equal to 0.5 Nm. Even if this bearing is on the flux of the forces, the preload on it is much higher than the external forces acting on the nut system. Thus, these variations will not have a big influence on the fixed bearing friction torque, being in this case possible to use the reference value.

As presented in chapter 3, on the test rig assembly two bearings of the model ZKLF3080-2RS-PE were used on the fixed side. In the Wälzlager Katalog (2014) exists a bearing of the type ZKLF3080-2RS-2AP-XL where the assembly is equal to two bearings of the type ZKLF3080-2RS-PE connected (Figure 27), but instead of the reference friction torque being double, it is 50 % higher.

In the Figure 27 is shown that the bearing model ZKLF3080-2RS-2AP-XL has the length equals to two times the length of the bearing model ZKLF3080-2RS-PE. Thus,

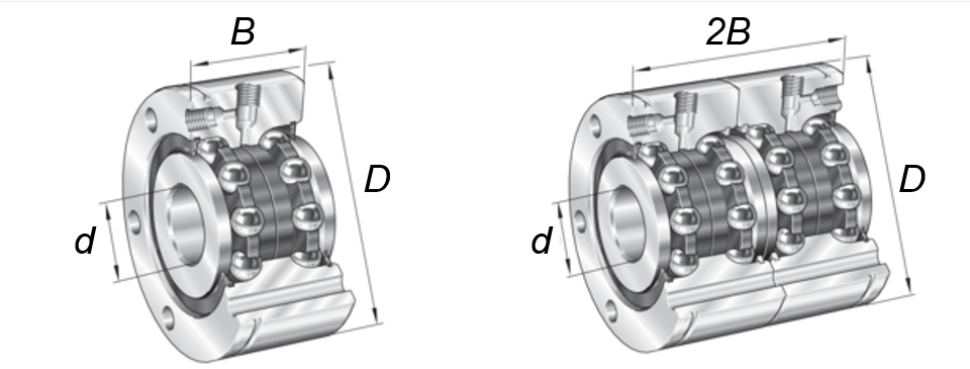

(a) ZKLF3080-2RS-PE. (b) ZKLF3080-2RS-2AP-XL.

Figure 27 – Different Bearing Models on the Fixed Bearing Assembly.

Source – Wälzlager Katalog (2014).

based on the reference values, the total friction torque acting on the fixed bearings can be 1 Nm, in the case that two ZKLF3080-2RS-PE are taken into account, or 0.75 Nm, for the case of the two ZKLF3080-2RS-PE being considered as one ZKLF3080-2RS-2AP-XL. Similar to the heat transfer coefficient for the conduction, the friction torque value for the bearings will be defined by the optimization process.

With the friction torque values defined, the heat generated is calculated based on Equation (35) and Equation (34), Mr_{bs} being the friction torque for the loose bearings and Mr_{bf} the friction torque for the fixed bearings. The calculated Mr_{bs} value is in Nmm, and the Mr_{bf} is in Nm. Therefore, the Mr_{bs} will be converted to Nm.

With the heat input calculated, it needs to be inserted in the system. In the thermal model geometry the bearings on the test rig are represented by solid dummies (Figure 28).

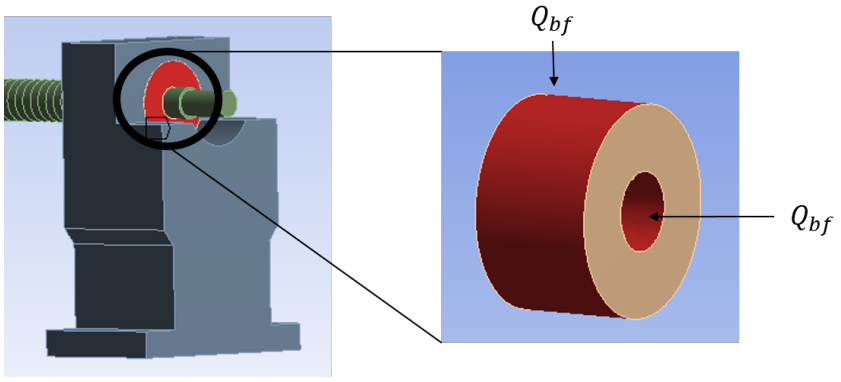

Figure 28 – Fixed Bearing Dummy Heat Input.

Source – Original.

Different from the previous version of the model, where the heat generated by the bearings was divided between the spindle and the support, and from Oyanguren

et al. (2018), where half of the heat is applied on the spindle and no bearings supports exists, the solution purposed in this work is that the heat is fully input on the bearing dummy, being half in the outer surface and half in the inner surface. In Figure 28 the heat input for the Fixed Bearing is represented, but the similar way is implemented for the Loose Bearing.

4.2.2 Nuts Heat Input

Regarding the nut-screw interface, the heat input is based on the model presented by Oyanguren et al. (2018), where the total friction was divided half to the spindle section and half to the nut. In the initial version of the model the nut was placed in the same position during all the simulation time, so a motion in the nut was implemented. At each iteration step, a nut middle position is calculated taking into account the speed, the travel length and the current time step. Since the portion of the spindle in nut travel length is divided in multiple PINs with the same area, and this area is lower than the area of the nut in contact, in each iteration step the heat is input in multiple PINs of the spindle (Figure 29).

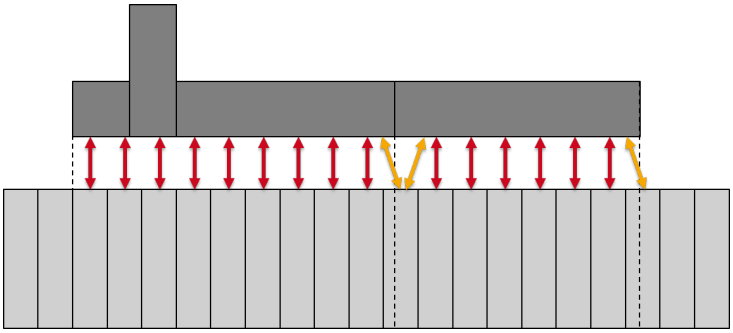

Figure 29 – Nut-Screw Interface Heat Input.

Source – Original.

During the nut travel some of the screw surfaces will not be a hundred percent in contact with the nut surface. This way just the percentage of the PIN in contact was taken into account. These partial heat inputs are described by the yellow arrows in Figure 29.

During the implementation of the nut travel, problems regarding to the PINs order were found. In the ANSYS geometry the PINs of the spindle are numbered from 0 to 155, this way the PINs are not imported by the Matlab code ordered by the position. Instead it is sorted by the number in the PIN file name as shown in Table 2. To solve this issue a MATLAB function that rearranges the PINs was implemented.

Position in ANSYS Geometry	Received Order in Matlab Code
1	1
2	10
3	100
4	101
⋮	⋮
13	11
14	110
⋮	⋮

Table 2 – PINs Order Issue.

Source – Original

4.3 POINTS OF INTEREST IN THE MODEL

Concerning to the thermal model the outputs that will be used in the coupling are the nodes temperature. With the aim to validate the thermal model developed with the test rig measurements it is necessary to find the nodes on the FEM mesh that match the sensors position in the test rig. Accordingly, node groups were defined and each group represents a sensor in the test rig. A simple algorithm takes the mean value of these nodes and stores for each iteration step of the simulation. The nodes index for each sensor can be found in Table 3.

Thermal Sensor Number	Assembly Group	Nodes Index in the FEM
T1	BG2	158, 164
T2	BG2	154, 163
T3	BG2	283, 277
T4	BG2	282, 273
T5	BG3	2114, 2076, 2083
T6	BG3	2316, 2284, 2300
T7	BG3	2314, 2292, 2285
T8	BG3	649, 654, 645
T9	BG3	84, 100
T10	BG3	76, 92
T13	BG3	1461
T14	BG3	1406, 1407, 1485
T15	BG3	3013, 3026, 3037
T16	BG3	3146, 3152
T17	BG1	105, ..., 130
T18	BG1	1, ..., 13, 27, ..., 39

Table 3 – Sensors location in the FEM

Source – Original

With the nodes for each sensor defined it is possible to compare the results properly. The presented step enables a proper comparison between the measured

values and the calculated ones.

4.4 CALCULATION PARAMETERS

As previously presented, doubts concerning to which value is to use for some of the model parameters exist. Also, some parameter values are based on models with different geometry than the one implemented on this work. Thus, to improve the thermal model results a parameterization, i.e., adjust the value of the parameters in the model, was performed. Based on Rocha (2020), where multiple optimization algorithms for a precision glass molding thermal model were compared and the Particle Swarm Optimization (PSO) was the algorithm that shows the better results, the PSO was chosen to perform the parameterization.

The PSO is a concept of optimization developed by Kennedy and Eberhart (1995). The algorithm uses multiple particles and moves them over the search space trying to minimize a cost function. The cost function:

$$Cost(parameters) = \sum_{k=1}^{n} MSPE(calculated(parameters)_k, measured_k)\,, \tag{49}$$

is the sum of the mean square percentage error (MSPE) between the thermal model points of interest and the sensors in the test rig with k being each sensor in the test rig. The MSPE is defined as:

$$MSPE = \frac{1}{n}\sum_{i=1}^{n} \frac{\left[y(i) - \hat{y}(i)\right]^2}{y(i)^2}\,, \tag{50}$$

where i is each iteration step in the thermal model, $\hat{y}$ is the model result and y is the test rig sensors value. Thus, closer the model results are from the measured data, smaller would be the MSPE value.

The search space are the parameters in the thermal model that will be optimized and they are shown in Table 4 and Table 5.

Heat Transfer Coefficient	Definition
$\alpha_{nutScrew}$	Coefficient between nut and screw
$\alpha_{nutCounternut}$	Coefficient between nut and counter nut
$\alpha_{nutSocket}$	Coefficient between nut and socket
$\alpha_{socketSupport}$	Coefficient between sockets and supports
$\alpha_{bearingsSpindle}$	Coefficient between bearing dummies and spindle
$\alpha_{bearingsSupports}$	Coefficient between bearing dummies and supports
α_{sink}	Coefficient between the supports and the ground

Table 4 – Heat Transfer Coefficient in the model

Source – Original

On Table 4 are presented the heat transfer coefficient in the conduction between different PINs that will be defined by the PSO, due the fact that, as already discussed, exist divergence in the literature value or do not are found in the literature, by the fact that the implemented FEM geometry implemented in this work is different than the presented in the literature.

Parameter Created	Definition
fixBearginFactor	Multiply the fix bearing heat input
looseBearginFactor	Multiply the loose bearing heat input
nutscrewFactor	Multiply the nut-screw interface heat input
internalConduction	Multiply the pure stiffness matrix in the FEM

Table 5 – Multiplier parameters in the model

Source – Original

On Table 5 are the parameters created to perform a fine-tuning on the heat inputs of the model and on the FEM matrix regarding the conduction in the same component.

The convection heat transfer coefficients were not optimized because:

- The coefficient values are calculated based on the VDI-Wärmeatlas (2013);
- The air data, e.g., thermal conductivity, viscosity, specific heat capacity, and so on, used to calculate the convection coefficients, are largely studied and its values can be trusted;
- The air data takes into account the temperatures of the environment and the components;
- Multiple convection coefficients are calculated in the thermal model, if all are optimized, the PSO complexity would increase unnecessarily.

The particles in the PSO will move in the search space combining the global and individual best costs. At each new position in the search space a cost function will be calculated, the global and individual best cost will be updated if it is the case and the next position will be calculated.

The size of the swarm was defined based on Cazzaniga et al. (2015) as

$$n = \left\lfloor 10 + 4 \cdot \sqrt{D} \right\rfloor , \tag{51}$$

where D is the number of parameters to be optimized and n is the number of particles in the swarm. As described by Kawakami and Meng (2009), in some PSO the particles can be trapped in a local minimum. To solve this a Particle Refresh was presented. This method was used in the PSO algorithm developed for this project.

Due to the fact that the PSO performs multiples times the cost function, and for a three hours simulation, i.e, 10800 iterations steps, the thermal model takes around 30

minutes to finish the simulation, with 11 parameters to be optimized, i.e., 23 particles, and considering that with 100 optimization steps a minimum cost will be found, as shown in Cazzaniga et al. (2015), the optimization would take around one and half months.

With all the presented considerations the following decisions were taken:

- Decoupling the bearings parameters optimization from the nuts parameters optimizations: this way the number of particles needed for each optimization will decrease, and the results become easier to analyse.
- Make $\alpha_{bearingsSpindle}$ equal to $\alpha_{bearingsSupports}$: this way one parameter for the optimization is removed and since in the bearings optimization the spindle temperature is not measured, $\alpha_{bearingsSpindle}$ becomes a loose parameter.
- Parallelize the optimization process: by doing this total time of optimization will decrease to two days.
- Increase the time increment of the thermal model: if a thermal increment of two instead of one is used the optimization time will decrease by half.
- Take into account multiple speeds during the optimization: thus the chosen parameters will ensure the robustness of the model.
- Use the experimental friction data from the test rig.

Regarding the decoupling, the only shared parameter is the *Internal Conduction*, the first optimization performed is the bearings one, and after this the parameter values will be fixed for the nuts parameters optimization. However, the *Internal Conduction* will be optimized again. If the *Internal Conduction* parameter became too different between the optimizations the decoupling approach will be disregarded.

For the parallelism implementation multiple computers were utilized. They were connected by an intranet and accessed a common file that stores the global best results of the swarm. To avoid conflict in the read of the file the data is written as a name of the file, since multiple threads are able to read the name of the file at the same time. If two files exist the thread that is reading will only consider the one with the lower cost. In the case of a new global best is found, a new file is created and the old one will be deleted, if it is not possible to delete the old file it will be left there because in the reading process this possibility is already managed.

For the bearings optimization the time increment considered was 10 seconds, but for the nuts optimization a higher value compromises the nut travel, in some cases the nuts position jumping from the same points during the whole simulation time. By this, for 500 RPM the time increment chosen was 6 seconds and for 1000 RPM the

time increment was 4 seconds. To ensure the robustness of the model the cost function was redefined as the sum of the MSPE for 500 RPM and the MSPE for 1000 RPM.

The values of the optimized parameters in the thermal model are shown in Table 6 and Table 7.

Parameter	Literature Value	Optimized Value
fixBearginFactor	1	1.514
looseBearginFactor	1	0.94
internalConduction	1	1.8265
$\alpha_{bearingsSpindle}$	-	2286 W/m^{2}K
$\alpha_{bearingsSupports}$	-	2286 W/m^{2}K
α_{sink}	-	323.82 W/m^{2}K

Table 6 – Bearings Parameters

Source – Original

Parameter	Literature Value	Optimized Value
nutScrewFactor	1	1.2298
internalConduction	1	1.8945
$\alpha_{nutScrew}$	300 W/m^{2}K	40 W/m^{2}K
$\alpha_{nutCounternut}$	2000 W/m^{2}K	2808.9 W/m^{2}K
$\alpha_{nutSocket}$	-	400 W/m^{2}K
$\alpha_{socketSupport}$	2000 W/m^{2}K	400 W/m^{2}K

Table 7 – Nuts Parameters

Source – Original

The overview of the parametrization results is the following:

- As informed in subsection 4.2.1, the fixed bearing friction coefficient value can be two times the reference value for the bearing ZKLF3080-2RS-PE (friction coefficient equal to 0.5 Nm) or the reference value for the bearing type ZKLF3080-2RS-2AP-XL (friction coefficient equal to 0.75 Nm). In the thermal model the friction coefficient was defined as one time the ZKLF3080-2RS-PE parameter. Being the *Fix Bearing Factor* result equals to 1.514, meaning that the coefficient used should be increased around 50 % and the correct bearing friction coefficient for the model is the ZKLF3080-2RS-2AP-XL parameter. After changing the friction coefficient the *Fix Bearing Factor* can be reset to one.

- The *Nut Screw Factor* result is higher than one, meaning that the values of the friction in the nut screw interface should be higher than the measured one. It can be explained by the fact that the friction torque measurement was performed without the tables and the nuts sockets, reducing the load on the nut and therefore reducing the friction measured.

- The *internalConduction* value in the optimization processes are close to each other. Thus, for the final result, the mean of the two results will be used, i.e., 1.8605.

To perform a comparison between the optimized parameters and the literature parameters, in the parameters that no value was found in the literature it was chosen to use 2000 W/m^{2}K.

To compare the results the following performance indices were selected:

- MPSE: mean square percentage error between the measured temperatures and the thermal model results as calculated in Equation (50). The smaller the better.
- Error %: Percentage error between the temperature measured and the thermal model results for the last instant of time calculated as

$$Error\ \% = \frac{\hat{y}(n) - y(n)}{y(n)} \cdot 100\% . \tag{52}$$

  As close to zero the better.

- Coefficient of Determination (R^2): this coefficient represents the correlation between the model and the measured data calculated as

$$R^2 = 1 - \frac{\sum_{i=1}^{n} \left[y(i) - \hat{y}(i)\right]^2}{\sum_{i=1}^{n} \left[y(i) - \overline{y}\right]^2} . \tag{53}$$

  According to A. Coelho and L. Coelho (2004), "an R^2 between 0.8 and 1 already reflects a sufficiently good identification in many cases". As close to one the better.

The performance indices for the bearings optimization and for the nut-screw optimization are shown in Figure 30 and Figure 31, respectively.

	Literature Value						PSO Parameters					
	500 RPM			1000 RPM			500 RPM			1000 RPM		
	MSPE	Error %	R^2	MSPE	Error %	R^2	MSPE	Error %	R^2	MSPE	Error %	R^2
T13	0.0028	-7.23%	-5.1114	0.00067	-3.72%	-1.9631	0.0013	-5.21%	-1.8021	0.00015	0.28%	0.3656
T14	0.0021	-6.47%	-2.9908	0.00009	-0.91%	0.6694	0.0014	-5.29%	-1.5421	0.00039	1.22%	-0.4148
T15	0.0078	-11.81%	-0.0697	0.0087	-11.98%	0.2305	0.0002	-2.66%	0.9703	0.00018	0.79%	0.9844
T16	0.0047	-8.78%	0.4070	0.0046	-7.85%	0.6192	0.0002	-2.01%	0.9745	0.00017	1.28%	0.9864

Figure 30 – Bearing Performance Indices.

Source – Original.

For the Bearings Optimization the sensors of the *Loose Bearing Support* (*T13* and *T14*) and of the *Fixed Bearing Support* (*T15* and *T16*) were utilized. For the sensors *T15* and *T16* the optimization process results in an improvement in all the performance indices and the R^2 calculated is in the specified range. Otherwise, for the sensors *T13* and *T14* the performance indices are improved but still the R^2 values are not between 0.8 and 1. It can be explained by the fact that since the temperature on both sensors do not increase too much (around 2℃), the environmental temperature changes during the experimental test and these changes are not taken into account in the thermal model, in the measured data of these sensor the environmental temperature will have a considerable effect. Being the difference between the measured and calculated values of the *Loose Bearing Support* sensors not big in magnitude, and these temperatures, for the coupling, not having a big influence, these values can be accepted.

	Literature Value						PSO Parameters					
	500 RPM			1000 RPM			500 RPM			1000 RPM		
	MSPE	Error %	R^2	MSPE	Error %	R^2	MSPE	Error %	R^2	MSPE	Error %	R^2
T1	0.0021	-6.34%	0.2249	0.0050	-9.36%	0.0171	0.00004	-1.30%	0.9843	0.00014	-2.00%	0.9713
T9	0.0016	-6.21%	0.4651	0.0040	-9.48%	0.2892	0.00037	-3.06%	0.8762	0.00095	-4.67%	0.8346
T6	0.00031	0.82%	0.8844	0.00035	-0.35%	0.9380	0.00012	0.91%	0.9543	0.00013	0.40%	0.9753
T7	0.00062	1.36%	0.7672	0.00089	0.43%	0.8467	0.00040	1.66%	0.8476	0.00062	1.46%	0.8876
T17	0.00042	-2.48%	0.7020	0.00078	3.25%	0.1643	0.00014	-0.5%	0.9072	0.00153	5.34	-0.6617
T18	0.00034	-2.04%	0.7423	0.00070	-0.26%	0.7392	0.00021	-0.23%	0.8387	0.00148	1.33%	0.4436

Figure 31 – Nut-screw Performance Indices.

Source – Original.

At the nut-screw optimization, the sensor from *T1* to *T10*, *T17* and *T18* are analysed. However, since some sensors are placed in similar position but in different tables and nuts, they are not presented in Figure 31. All performance indices, excepted for the screw temperatures (*T17* and *T18*) at the 1000 RPM, were improved. Regarding the screw temperatures at the 1000 RPM the performance indices are worse due to the fact that in this test the thermal camera moved slightly to a different point in the spindle height and the data collected was interpolated between the correct measurement points, thus resulting in wrong measured values. With these results it is possible to conclude that the data from the thermal camera is very sensitive and as already presented in the chapter 3 that the accuracy of the data is ± 2 ℃ these differences in the performance indices are expected.

In Figure 32 are presented the measured and calculated temperatures for sensors placed on the nut (T1), on the nut socket (T9) and on the tables (T6) at 500RPM

and 1000 RPM. The places of the sensor can be found in Figure 21.

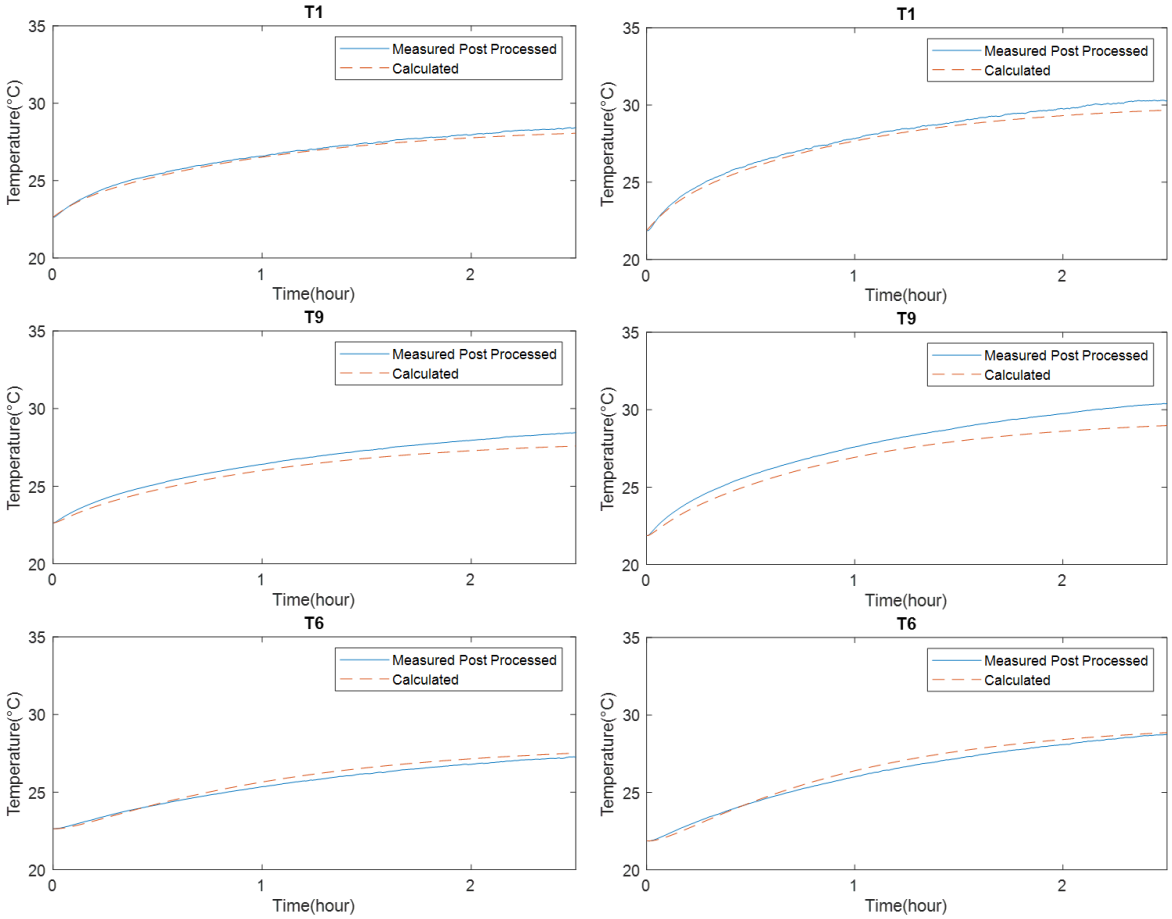

(a) Results for 500RPM.

(b) Results for 1000RPM.

Figure 32 – Measured and Calculated Temperatures of the Nut.

Source – Original.

The calculated values for *T1* and *T6* are close to the measured data. Concerning the *T9* a small difference is verified, but since the temperature used in the coupling of the models will be only the nuts and the screw temperatures, these small differences on the other sensors can be accepted. This difference on the *T9* can be noticed on the R^2 values in the Figure 31, being the Coefficient of Determination for this sensor further from one than the sensors *T1* and *T6*.

5 MECHANICAL MODEL MODIFICATION

In order to connect the models the MTPlus software was modified. The implemented modifications will be divided in two chapters. This chapter is focused on the mechanical models implementations, being it the frictions model added to the main model. The next chapter is focused on the changes of the workflow of the MTPlus to connect it to the thermal model.

In this chapter the implementations of the frictions model developed by Steinert (1995) and the friction model developed by Olaru et al. (2005) will be presented. The model results are compared to the experimental Stribeck Curve measured on the test rig. At the end, an overview concerning the model results is discussed.

5.1 STEINERT FRICTION MODEL

As already introduce in the State of the Art the Steinert Friction Model was developed and validated for bearings. It is important to mention that some calculations of this model were already implemented in the MTPlus, these being the Hertzian Contact Characteristics and Lubrication Film Conditions. The Hertzian Contact Characteristics calculations were already validated by Brecher et al. (2018) by comparing the results of the displacement in the model with measured data.

In Figure 33 are presented the inputs, outputs and the parameters of the lubricant film conditions and Steinert Friction calculation.

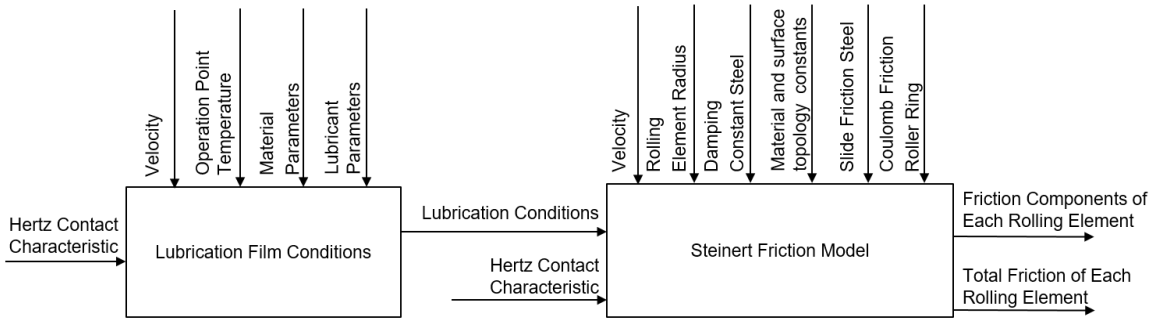

Figure 33 – Lubrication Film Conditions and Steinert Friction Systems Representation.

Source – Original.

The Hertz Contact Characteristics of the model are the Maximum Contact Pressure, the minor and major axis of the contact ellipse, the normal load and the contact angle. In the lubrication conditions are the lubricant film height and the dimensionless speed parameter U, dimensionless material parameter G and the dimensionless load parameter W. Regarding the parameters of calculation, the velocity parameters are the screw rotational speed and the angular roller speed. In the material parameters is the

Young's Modulus E. The material and surface topology constants are the ones used, with the lubrication film height, to determine the percentage of each kind of friction in the total friction calculation as demonstrated in Equation (8) and Equation (9).

In Figure 34 are the calculated frictions for different speeds when there is no external load in the system and when the external load is 6000 Newtons.

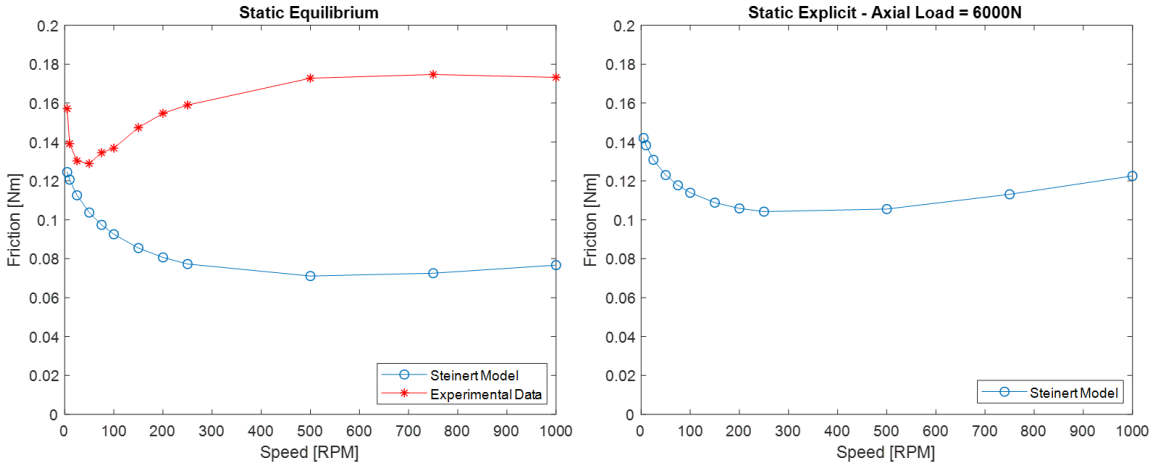

Figure 34 – Steinert results with and without external load.

Source – Original.

The model result is compared with the experimental data in the case of no external load in the system. It is possible to verify that the calculated friction is smaller than the measured data. By comparing the model results with and without external load, it is possible to check that with an external load in the system the calculated friction will be higher, since when the load is applied the normal forces acting on the rolling elements tend to increase.

In Table 8 are the parameters used in the Steinert Friction model.

Parameter	Value	Parameter	Value
Young's Modulus	210000 N/mm^2	Roughness Roller	0.107 µm
B	0.9	Roughness Ring	0.15 µm
C	1.0	Slide Friction Steel	0.1
Lubricant Density	$8.76 \cdot 10^{-7}$ kg/mm^3	Coulomb Friction	0.1
Kinematic Viscosity	216.86 mm^2/s	Damping Constant Steel	0.7 %
Temperature	20 °C	Rolling Element Radius	3 mm

Table 8 – Parameters for Steinert Friction Calculation

Source – Original

The material and surface topology constants, B and C, the roughness of the components, the slide friction steel, the Coulomb friction and the damping constant steel was extracted from Steinert (1995). The density and the kinematic viscosity of the

lubricant oil are parameters of the lubricant *Shell Tonna S3 M68* used in the test rig at 20 °C.

With the aim to improve the calculated results, the components of the friction and the percentage factor λ of CSB and EHD for the mixed regime needs to be studied and the calculated values for different speeds are presented in Figure 35.

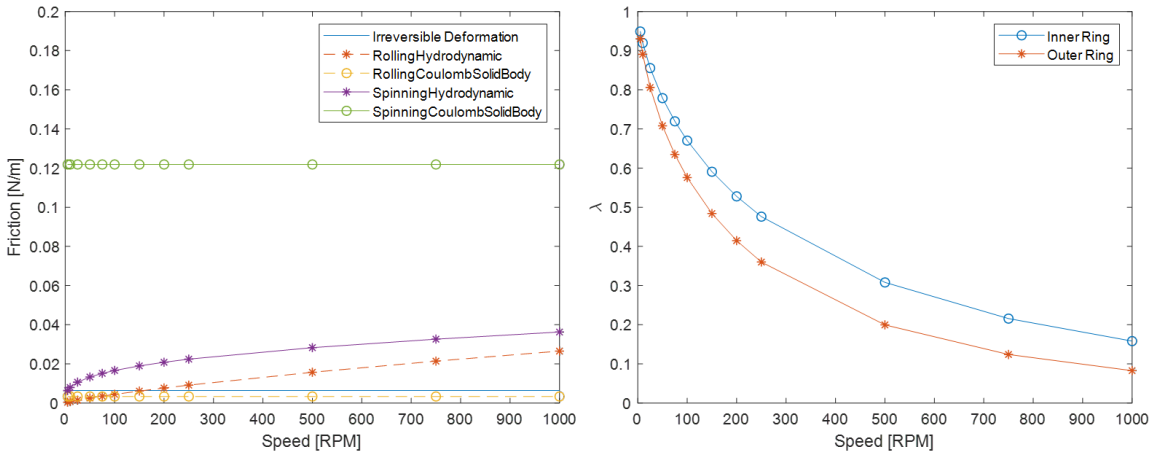

Figure 35 – Friction Components and λ over speed changes.

Source – Original.

Analysing the Figure 35 is possible to conclude that the λ is inversely proportional to the rotational speed of the shaft. So, in lower speeds the CSB friction components will have higher influence on the calculated friction and with higher speeds the EHD friction components will dominate the total friction in the system.

To make the calculated results closer to the experimental data the Slide Friction Steel and the Coulomb Friction was changed from 0.1 to 0.13 and the calculated results are in Figure 36.

With the changes in the parameters the values of the CSB friction components have been raised, resulting in a increase of the friction on lower speeds. Thus, the starting point of the calculated slope matches the experimental data.

It is important to remember that in the original model by Steinert (1995) a component for the cage friction with the rolling elements and with the inner and outer ring is calculated, however in the ball-screw system there is no cage, so this component was disregarded, instead, in the ball-screw rolling elements a ball to ball friction will occur. Therefore, for future works, the ball to ball friction can be introduced in the Steinert (1995) Friction Model to the calculated results match the experimental data. The parameters regarding the material and surface topology, i.e, *B*, *C* and the roughness of the components, can be modified.

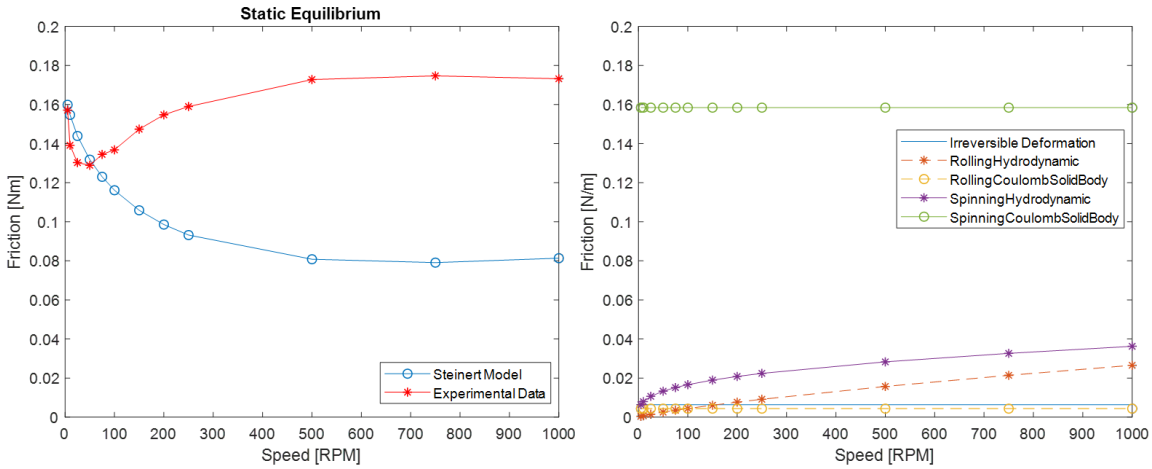

Figure 36 – New CSB parameters Results

Source – Original.

5.2 OLARU FRICTION MODEL

Diverging from the approach to the Steinert Model implementation, in this Friction Model, instead of using entirely the Contact Characteristics from MTPlus, the calculations regarding the minor and major axis of the contact ellipse are calculated in the model and they are based on Olaru et al. (2005). With this approach the inputs, outputs and parameters of the model are presented in Figure 37.

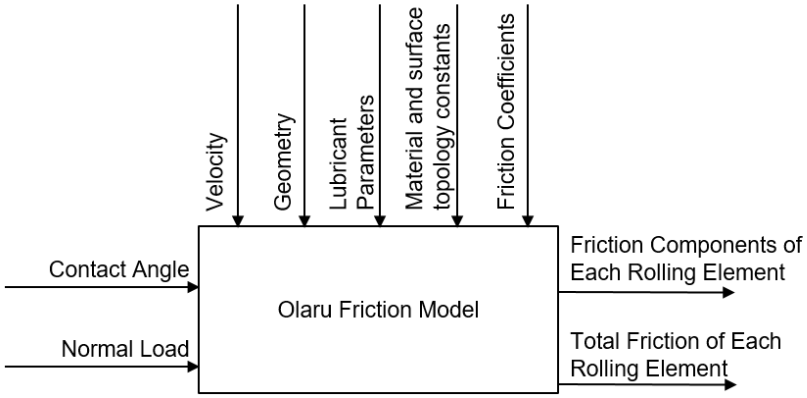

Figure 37 – Olaru Friction Model Representation.

Source – Original.

With respect to the parameters of the calculations, the *Geometry* includes the screw radius, the lead radius, ball radius and the number of rolling elements on the nut-screw interface. The others parameters are similar to the ones described in the previous section with different values. The *Friction Coefficients* includes the μ_0 and

the *Friction Coefficients of the Balls*. The literature parameters values are presented in Table 9.

Parameter	Value	Parameter	Value
Young's Modulus	210000 N/mm^2	Roughness Roller	0.08 μm
B	1.42	Roughness Ring	0.3 μm
C	0.8	Slide Friction Steel	0.1
Lubricant Density	$8.76 \cdot 10^{-7}$ kg/mm^3	Number of balls	168
Kinematic Viscosity	216.86 mm^2/s	Friction Coef. of the Balls	0.1
μ_0	0.2	Rolling Element Radius	3 mm
d_m	40 mm	d_w	3.022 mm

Table 9 – Parameters for Olaru Friction Calculation

Source – Original

With these values the friction is calculated with no external load applied on the system. The results of the friction compared to the experimental data and the behavior of the friction coefficient calculated in Equation (10) for different speeds are presented in Figure 38.

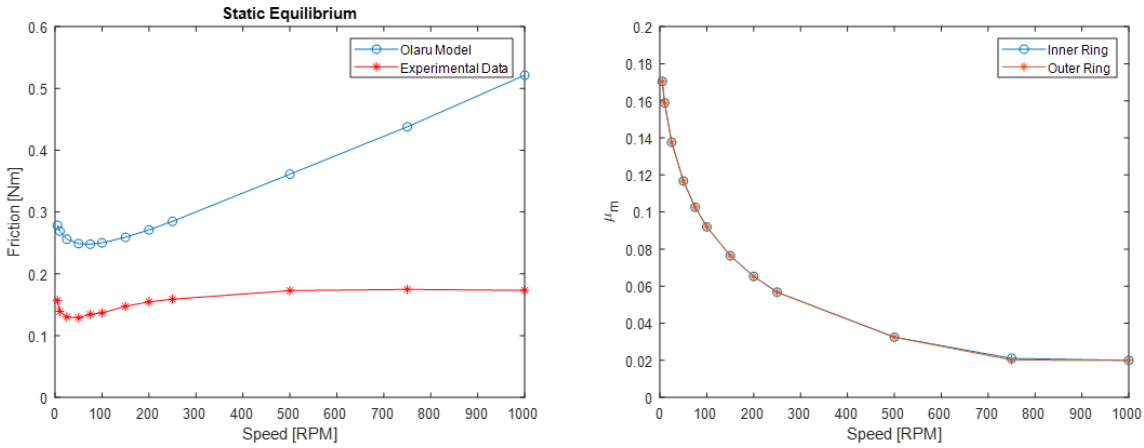

(a) Olaru Result. (b) Friction Coefficient over speed changes.

Figure 38 – Olaru Friction Model with Literature Parameters

Source – Original.

The variation of μ_m by the speed changes in Figure 38b is similar to the slope of the percentage factor of CSB and EHD in the Steinert Model visualized in Figure 35. Different from the Steinert Model, in Figure 38a the values are higher than the measured ones, so, as previously done, the approach is to reduce the coefficients that affect the friction when the lubrication film height is low, in this case it will be the μ_0. By decreasing the parameter μ_0 from 0.2 to 0.1, the new model results are shown in Figure 39.

Equally as done in the previous model, the Friction calculated at lower speeds is close to the Experimental Data.

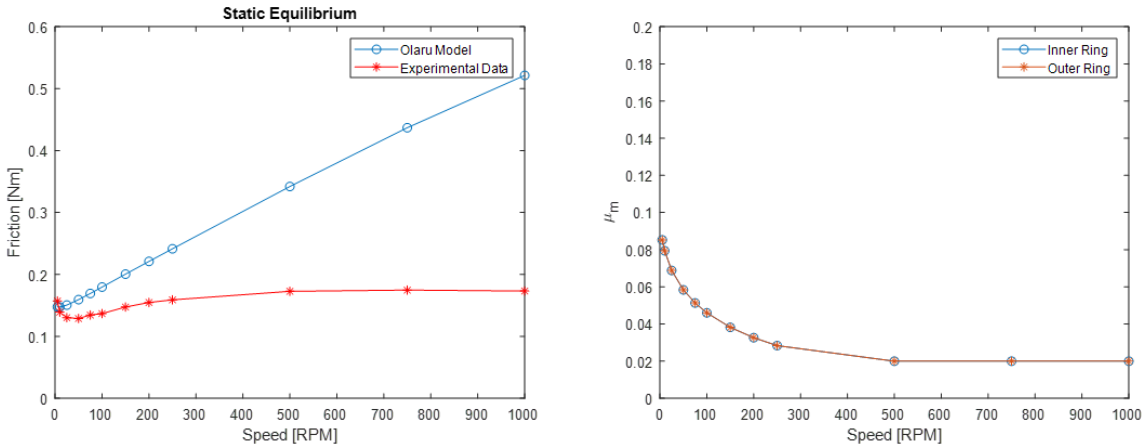

(a) Olaru New Result. (b) Friction Coefficient over speed changes.

Figure 39 – Olaru Friction Model with Modified μ_0

Source – Original.

5.3 FRICTION MODELS OVERVIEW

Both friction models presented on this project show acceptable results for lower speeds. As the speed increases, the friction goes from the boundary lubrication regime to the mixed regime and then to the hydrodynamic regime. At this moment, the behavior of the friction models is distinct, as the Steinert Model values are below the Experimental Data, and the Olaru Model values are above the Experimental Data.

With respect to the Steinert Model, the Friction Components that start having higher influence in the total friction calculated at higher speeds are the EHD components. The Rolling fluid friction force F_{EHD} calculation are shown in Equation (18) and Equation (19). The fluid friction coefficiet μ_{EHD} in Equation (19) will increase with an increase in the speed parameter and decrease with an increase on the load parameter or on the material parameter. These parameters are calculated on the Lubrication Film Conditions shown in Figure 33. The speed parameter is dependent on the Lubricant Parameters, the Velocity, the Material Parameters (Young's Modulus) and the Hertz Contact Characteristics. The load parameter is dependent on the Hertz Contact Characteristics and Young's Modulus. The material parameter is dependent on the Young's Modulus and the Lubricant Parameters. Since the Hertz Contact Characteristics was validated by Brecher et al. (2018), the parameters that should be better studied are the Young's Modulus and the Lubricant Parameters.

The Drilling fluid friction torque M_{EHD} on Equation (23) is dependent on the drilling speed, the lubricant film height and the viscosity function integrated over the contact ellipses. The lubricant film height is dependent on the speed parameter, the load parameter, the material parameter and the Hertz Contact Characteristics. With an increase of the speed parameter or the material parameter the lubricant film will

increase and the drilling fluid friction torque will decrease, and the opposite is true for the the load parameter. The drilling speed is dependent on the speed and the geometry of the ball-screw calculated and these values are based on the experimental test rig assembly. The viscosity function is computed on the Lubrication Film Conditions show in Figure 33 and it is dependent on the Lubricant Parameters and the Hertz Contact Characteristics. Thus, as mentioned for the fluid friction force, the Young's Modulus and the Lubricant Parameters should be better studied.

Regarding to the Olaru Model, as shown in Equation (30), the friction force is composed of hydrodynamic rolling force and the sliding forces. The hydrodynamic rolling force is dependent on the Young's Modulus, the geometry of the ball-screw, the speed parameter, the load parameter and the material parameter. With an increase of the the speed parameter, the load parameter or the material parameter the hydrodynamic rolling force will increase. The calculation of these parameters and the considerations concerning to it are similar to the ones already presented in the Steinert Model, regarding the fact that instead of using Hertz Contact Characteristics calculated on MTPlus it uses the transversal equivalent radius, dependent on the geometry, calculated on the model. Therefore, equally as discussed on the Steinert Model overview, the Young's Modulus and the Lubricant Parameters are the key parameters for an improvement in the model.

The sliding forces calculated in Equation (27) and Equation (28) are dependent on the geometry, the Ball-to-Ball Friction Force and Moment, the hydrodynamic rolling force, the curvature friction moment and the elastic resistance in the ball-groove contact. Ball-to-Ball Friction Force is a constant of the model and the Ball-to-Ball Friction Moment is dependent on this constant and the parameter *Friction Coef. of the Balls* presented in Table 9. Thus, these should be the parameters best studied. The curvature friction moment calculated on Equation (29) is dependent on the geometry, Hertz Contact Characteristics, contact load and the friction coefficient calculated on Equation (10). Since with the increase of the speed this coefficient decreases, these moments will not have a large influence at high speeds, thus, its analysis may be disregarded. The elastic resistance, as shown in Olaru et al. (2005), is dependent on the contact load, the geometry and the Hertz Contact Characteristics calculated on the model. The Contact Characteristics on the model are dependent on the geometry, the contact load and the Young's Modulus. Thus, as the geometry is dependent on the test rig, the contact load calculated on MTPlus was already validated, the parameter to be modified is the Young's Modulus.

6 THERMO-MECHANICAL COUPLING IMPLEMENTATION

As the thermal model was developed to be connected with the mechanical model, the implementations concerning to the thermo-mechanical coupling were performed on the mechanical model.First, the new geometry implemented on the MTPlus is presented. Afterwards, an interface to define the calculation parameters of the thermal model is exhibited.

As the elements used in the FEA are distinct between the models, a mapping process to input the element temperatures in the mechanical model from the nodes temperature in the thermal model was developed.

The MTPlus is a structural stiffness simulation software. Thus, the thermal difference between the components and the environment needs to be converted into equivalent axial forces. The functions for this conversion will be addressed in this chapter.

In the previous MTPlus version all the temperatures to forces conversion were done in the Preprocessor step and these forces were applied in the system on the Static Equilibrium calculation job. However, as the idea of this project is to use the mechanical results as an input for the thermal model and then use the thermal model results as an input on the mechanical model, the mechanical model needs to be calculated previously as the external temperatures being inserted on it. Thus, it is necessary to modify the working flow of the mechanical model.

With the appropriate implementations considered, the coupling results will be presented. The relative displacement between the nut and the spindle on the test rig is measured, then, the mechanical model displacement calculated will be compared to the experimental data.

A consideration concerning the friction models results is needed. Since both the friction models implemented do not give acceptable results for the velocity at which the experimental measurements were performed, it was chosen to use the Stribeck Curve measured on the test rig to validate the thermo-mechanical coupling.

6.1 MTPLUS GEOMETRY

With the aim to compare the MTPlus results with the experimental measurements, the geometry was based on the test rig assembly and is displayed on Figure 40.

Different from the thermal model geometry, in MTPlus the screw and the test nut are implemented. In this geometry the support nut is not considered. The rolling elements are presented in this geometry, since they are one of the objects of study in the mechanical model. At the motor side a holder keeps the spindle in place. As presented on the State of the Art, on the model implemented the spacer of the nut is replaced by a spring with extremely high stiffness.

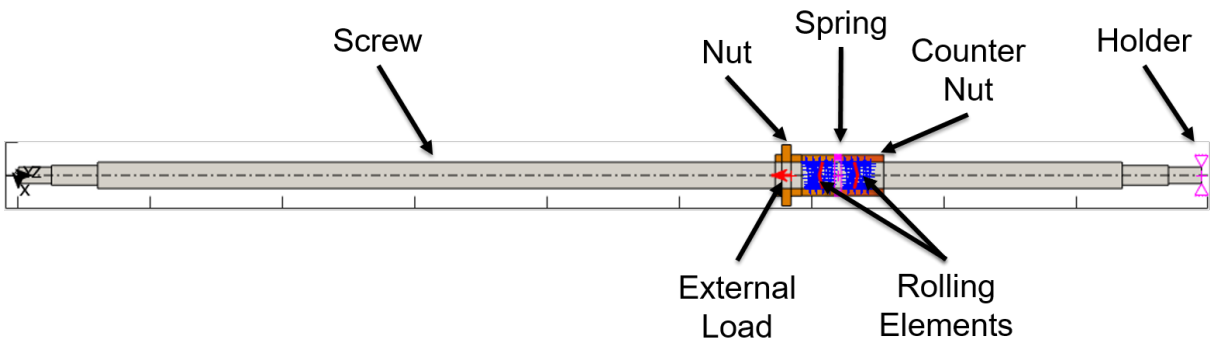

Figure 40 – MTPlus geometry.

Source – Original.

6.2 THERMAL MODEL INPUTS INTERFACE

All the thermal model definitions would be done in the mechanical model, since this is the model that the end user will have access to. Therefore, an interface to define the thermal model parameters was developed on the MTPlus an it is shown in Figure 41.

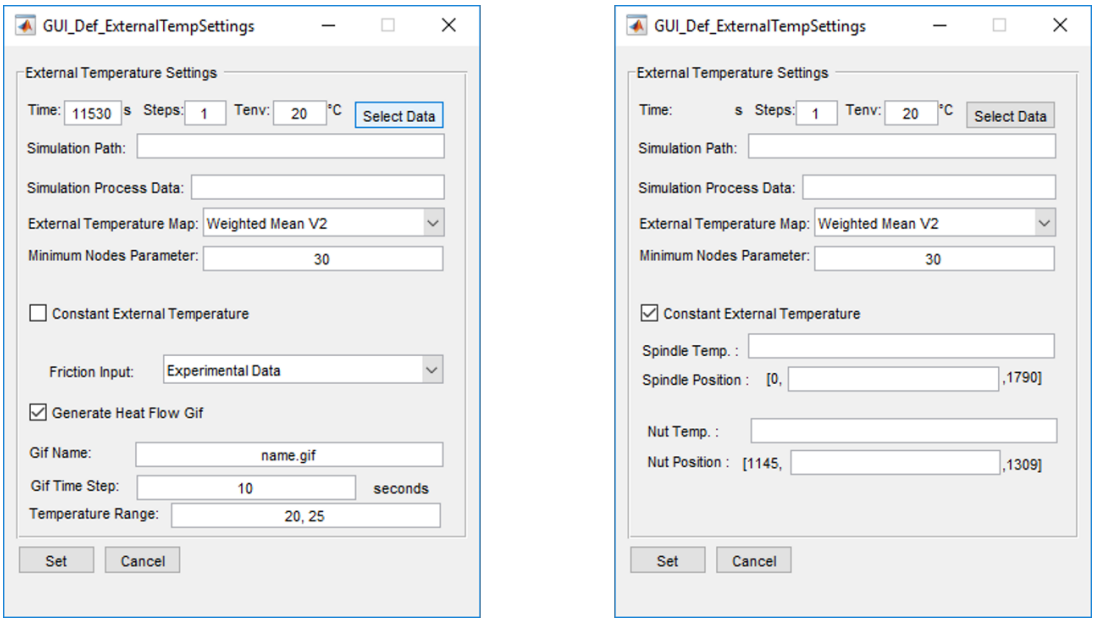

Figure 41 – MTPlus User Interface for the thermal model definition.

Source – Original.

On the user interface for the thermal mode are defined the simulation time, the number of iteration steps in the thermo-mechanical coupling, the Environment Temperature, used to match the calculated results with the test rig results, the simulation path of the thermal model, simulation process data of the thermal model, it being a *XLS* file where the simulation time and the rotational speed will be used by the

thermal model, the External Temperature Map and its calculation parameter, Minimum Nodes Parameter. With the aim to validate the external mapping developed, a *Constant External Temperature* can be defined, when it is selected the mechanical model will run the thermal model for only iteration step and will change the calculated temperatures for the constants values defined by the user. In the Friction Input is defined with friction will be used in the thermal model, being it the Experimental Data from the Stribeck Curve measured or the MTPlus Data from the Frictions Models presented in the previous chapter.

On this user interface it is possible to create a *GIF* with the thermal results from the thermal model. A frame of the generated *GIF* is displayed on Figure 42.

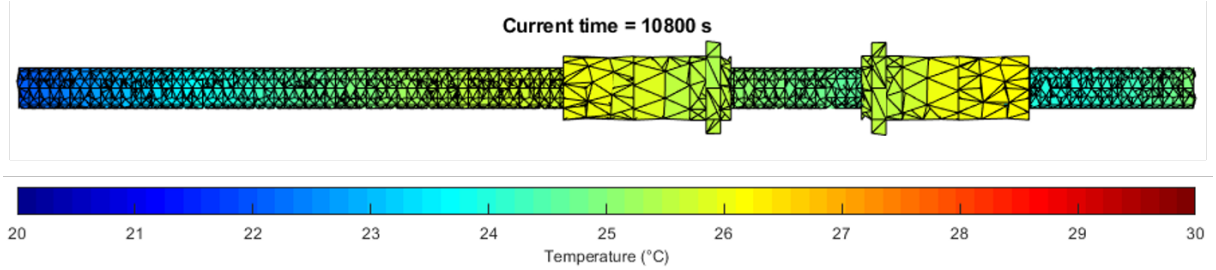

Figure 42 – Frame of the GIF generated with the Thermal Model Geometry and Result.

Source – Original.

To generate the *GIF* it will be plotted the thermal model Geometry and the Temperature Results at each iteration step of the thermal model. Since some parts of the model heat up more than others ones, and for the connection between the models is interesting to visualize the temperature in the nut and in the spindle over the travel length, it is possible to define a temperature range in the *GIF*, thus the points of interests can be better visualized. In the *GIF* Time Step is possible to define the time steps between the *GIF*s frames, by using this it is possible to visualize the evolution of the whole simulation in a short period of time in the *GIF*.

6.3 EXTERNAL THERMAL MAP

As presented in the State of the Art, and shown in Figure 43, the Finite Element mesh is different between the models due to the fact that they use different elements in the FEA. The thermal map is implemented with the aim of enabling the mechanical model to use the thermal model results.

On the MTPlus a thermal mapping was implemented on the prior version but it does not fit the new geometry implemented. It happens by the fact that in the previous approach the Mechanical Model elements temperature were defined as the mean of the thermal model nodes temperatures contained in the element length, but for the

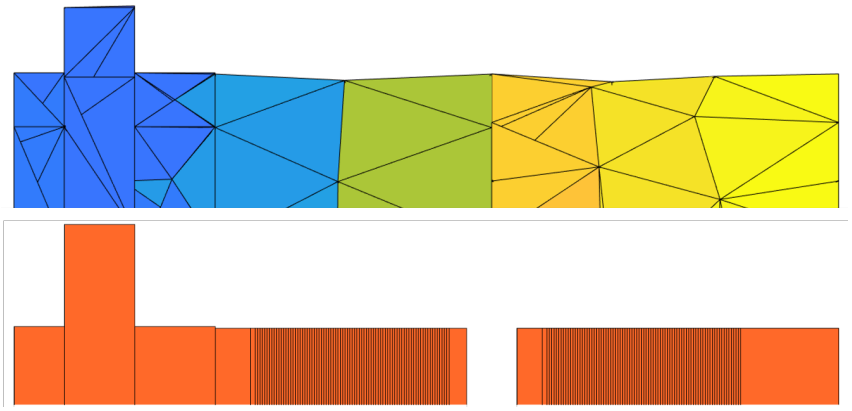

Figure 43 – Comparison of the mesh between the models.

Source – Original.

geometry used in this work for some elements in the mechanical model there are no nodes corresponding in the thermal model. Thus, different approaches for the thermal mapping were developed and are presented in the sequel. For a better explanation of the approaches, *nodes* will refer to the thermal model FEA nodes and *elements* will refer to the mechanical model FEA elements.

- **Interpolation:** in this approach, if the amount of nodes contained in element's length is equal or higher than the minimum nodes parameter defined the element temperature will be calculate as a mean of the nodes. Otherwise, if the number of nodes is lower than the parameter, the temperature of the element will be Interpolated. It is import to emphasize that for the first and last element the minimum node value will be not respect by the fact that the interpolation needs at least two values to be performed.

- **Node Average:** in this mapping the calculation will be made the same way as in the Interpolation approach, regarding to the fact that the minimum node value will not be used, by this if a single node is find in the element's length the element temperature will be the node temperature.

- **Weighted Mean:** if the number of the nodes in the element length is lower than the minimum node parameter, the search space will be increased by the element length in a iterative way until the number of nodes found be equal or higher than the minimum node parameter. With the corresponding nodes, instead of take the mean value as it was done in the previous approaches, the distance between the founded nodes and the element will weight the calculation

- **Weighted Mean V2:** the idea of this mapping is the same as the weighted mean, but in this approach, after the minimum nodes parameter be found, if exist multi-

ples nodes in the same Z-axis point, the mean of it will be calculated and these nodes will be considered as just one node during the weighted mean calculation.

In Figure 44 the difference between the mappings with minimum node parameter equals to 30 is shown. The thermal model simulation was performed with three hours simulation, a single step and environment temperature equals to 20°C.

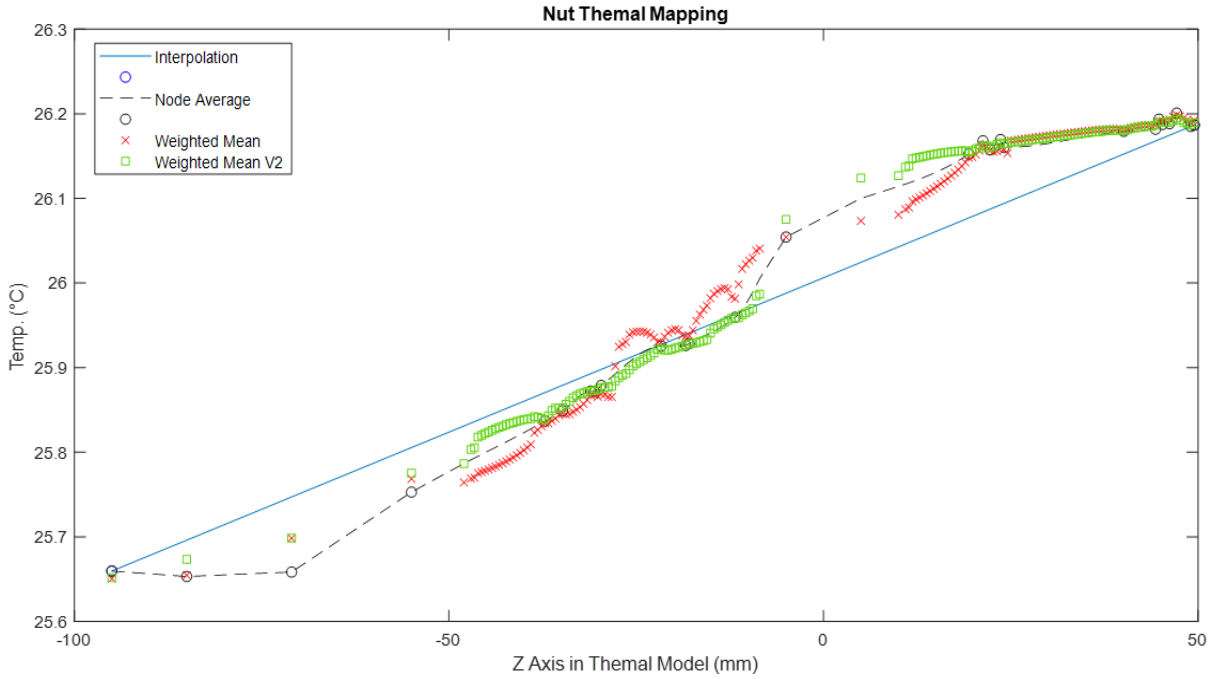

Figure 44 – Nuts Mapping Results.

Source – Original.

Analysing the mapping results for the nuts is possible to verify that for the *Interpolation* approach the elements temperatures was mostly the result of the interpolation of the temperatures at the starting and ending point of the nut. It happens because in the nuts most of elements do not have on it length the minimum node corresponding.

The other three approaches purposed are able to map the thermal variation on the nut lenght, for the *Node Avarage* at some elements the interpolation is still performed. The *Weighted Mean* present, at the Z position of -30 mm to -10 mm, a kind of oscillatory behavior differently from the others approaches. The *Weighted Mean V2* shows a more smooth slop than the *Weighted Mean* but still is able to get temperature variations between the components better than the interpolation performed by the *Node Avarage*.

With the mapping performed, the element temperatures are stored in an array for each element, being the first value the defined temperature for the components in the MTPlus, and the following values the calculated mapping temperature minus the environmental temperature defined in the User Interface shown in Figure 41 added

to the first array value. Thus, the mapping result will be the initial temperature of the component added to the thermal difference calculated by the thermal model.

When a single connection between the mechanical and thermal models are performed the resulting array will have two values, otherwise, if multiples connections occurs the resulting array will have the current connection step plus one values stored (the array size will increase in each coupling iteration).

6.4 MECHANICAL MODEL WORKING FLOW MODIFICATION

As displayed in the State of the Art, Oyanguren et al. (2018) developed two different approaches for the thermo-mechanical models coupling, the Non-Updated Heat (NUH) and the Updated Heat (UH). In this final project work both approaches was implemented and will be presented in this section. The kind of coupling approach is defined in the User Interface shown in Figure 41, if the *Steps* parameters is defined as 1, the NUH will be used, otherwise, if this values is higher than 1, meaning that multiples connections between the models will be performed, the calculation approach is the UH one.

For both calculation approaches is possible to use as the *Friction Input* the *Experimental Data* or the calculated friction in MTPlus. If in the parameters of the MTPlus calculations multiples external load inputs are selected (*Static Explicit* and *Static Implicit*) a pop-up window will be created for the user defines which External Load Results will be used to calculate the friction. If none is selected the MTPlus will use the *Static Equilibrium* results for the friction calculation. In the case that only one external load input is selected, or no external load is selected, or the *Friction Input* for the thermal model is the *Experimental Data* no pop-up window will be displayed.

In the sequel, first, the conversion of the element temperatures to forces that act in the system are addressed, following by the Non-Update Heat and Updated Heat implementation.

6.4.1 Thermal Forces

As previously described, with the element temperatures, thermal forces will be calculated and applied in the system. On the prior version of the MTPlus software the differences of temperature of the components defined as a parameter are computed as thermal forces on the beam elements as

$$\text{Thermal Force} = \text{Thermal Expansion} \cdot \text{Temperature Difference}\,, \tag{54}$$

and the thermal expansion was determined as

$$\text{Thermal Expansion} = E \cdot \alpha_T \cdot A\,, \tag{55}$$

using the Young's Modulus E, the coefficient of thermal expansion of the material α_T and the cross section area of the element analysed A.

These previous calculations are all performed on the Preprocessing step of the MTPlus. In the implemented version of the MTPlus, the thermal mapping will be performed on the calculations jobs and after it, instead of having a single temperature for the elements, an array will be storing the iterations temperatures. Thus, modifications on the calculation approach are necessary.

The Thermic Load Substitutes function is the one that will convert the differences of the temperatures between the components into thermal forces. From the Equation (54) and Equation (55) the Forces action in each element in the mechanical model are

$$F_T = E \cdot \alpha_T \cdot A \cdot \Delta T\,. \tag{56}$$

The literature value for E is equal to 210 GPa and for α_T the value is $11.6 * 10^{-6}$ m/mK. The Cross Section Area A is geometry dependent.

In the State of the Art was exposed that the Beam Elements in the FEM have 6 degrees of freedom, and being the Thermal Forces just acting in one of this degrees of freedom, the functions calculation the thermal forces handle it.

In Figure 45 are present the steps of the calculation of the Thermal Forces.

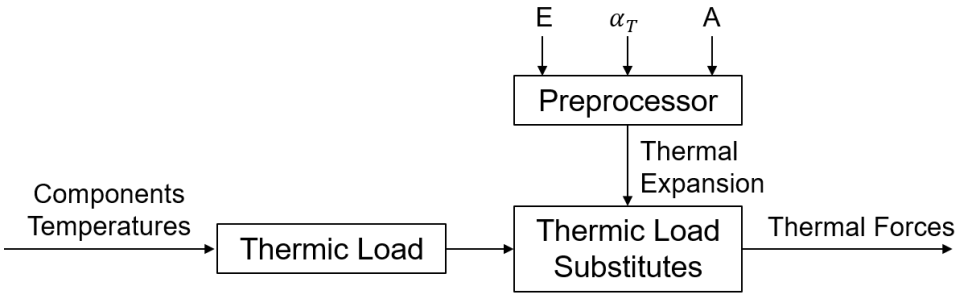

Figure 45 – Thermal Forces Calculation.

Source – Original.

First, in the Preprocessor step, a Thermal Expansion vector will be generated with length equals to the number of elements in the mesh times the degrees of freedom. For the degree of freedom affected by the thermal forces the calculation is presented in Equation (55) and for the others degrees of freedom the value is Zero. A Thermic Load array is calculated using the components temperatures. The first column of the Thermic Load will be the difference between the first temperature of the componenets and the standard temperature of the MTPlus (20 ℃). The following Thermic Load will be the current element temperature minus the previous temperature.

In the case that the UH coupling approach is selected at each iteration a new temperature will be added to the element array, therefore, a new column will be added to the Thermic load matrix. The Thermic Load function places the temperature differences in the right degree of freedom.

At last, the Thermic Load Substitutes calculation is performed. For each element it is defined as

$$TLS = \frac{TE}{2} \cdot (TL_{n-1} + TL_n) - \frac{TE}{2} \cdot (TL_n + TL_{n+1}), \tag{57}$$

being TLS the Thermic Load Substitutes, TE the Thermal Expansion and TL_n, TL_{n-1} and TL_{n+1} the current, the previous and the next elements Thermic Load, respectively. The thermal forces calculated for the elements will counteract each other, this is because the element will expand in both directions horizontally.

6.4.2 Non Updated Heat

The NUH is an approach in what the connection between the model occurs just one time. This calculation approach takes less computing time, due to the fact that the selected calculation jobs will be computed at the maximum of two times. It is indicated when the Friction Input selected is the Experimental Data and only the final result of the mechanical model is necessary.

The NUH working flow is displayed in Figure 10.

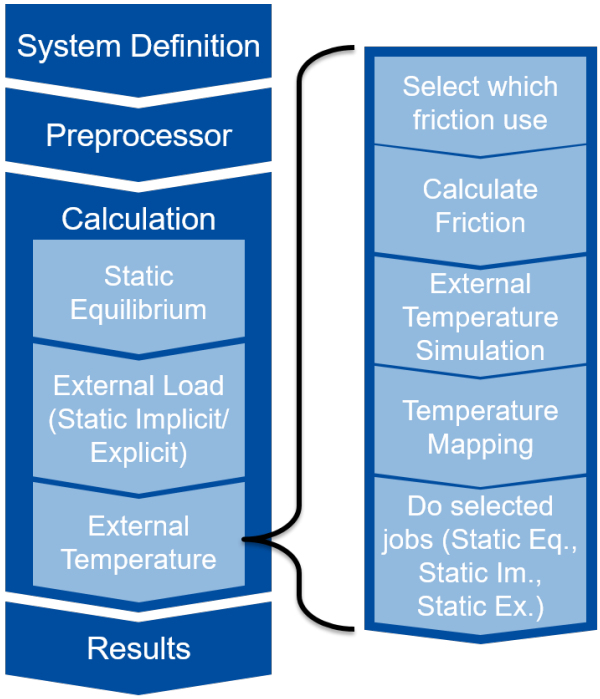

Figure 46 – Non-Updated Heat working flow.

Source – Original.

First, the whole mechanical model is solved for the user defined parameters. Considering the case that the external temperature is selected, the MTPlus will check if it is necessary to calculate the friction using the mechanical results or not. If the friction calculation is necessary, the MTPlus will verify which friction model use and will calculate it, otherwise, the Calculation Friction step will be skipped.

With the friction and the other defined parameters of the thermal model defined the External Temperature Simulation is performed. When the thermal model calculation is over, the mechanical model will use it results to calculate the Thermal Map and the Thermal Forces acting in the system.

With the thermal forces, the system will do the selected jobs again, being the external thermal forces used in the *Static Equilibrium Thermic* as shown in Figure 10.

An important consideration about this working flow implemented is that if the *Friction Input* selected is the *Experimental Data*, the first solving of the mechanical model will be useless, since it is only used for the friction calculation.

6.4.3 Updated Heat

The UH is an approach in what the connection between the model occurs multiples times. This calculation approach takes more computing time, since the selected calculation jobs will be performed the number of selected steps plus one. This calculation approach is useful when the Friction Input selected for the thermal model is the result of one of the friction models. Thus, the thermal forces of each iteration will be applied in the system, changing the Contact Characteristics of the rolling elements and modifying the friction values calculated. Even with the Experimental Data for the friction this approach is interesting, by the fact that it enables to study the behavior of the mechanical model results at each coupling iterations step.

On Figure 47 are presented teh working flow of the MTPlus when the Update Heat approach for the themo-mechanical coupling is selected.

Similar to the NUH, the UH will first solve the whole mechanical model before start the external temperature iteration and the work flow is almost similar, differing by the fact that the External Temperature Simulation will be performed multiple times.

Differently from the NUH, in this coupling approach the mechanical will not be solved completely when a new *External Temperature Simulation* step is performed. Since it is in the *Static Equilibrium* job where the thermal forces are applied in the system, the results of this job will be stored and used as a starting point for the next iteration. Considering that for each coupling iteration a new value is appended in the elements temperatures array, resulting in a new column in the Thermic Load Substitutes, if the mechanical model is fully solved, a linear increase of the calculations steps for the External Temperature will result in a exponential increase of the number of equilibrium's calculated and consequently a exponential increase in the computing time.

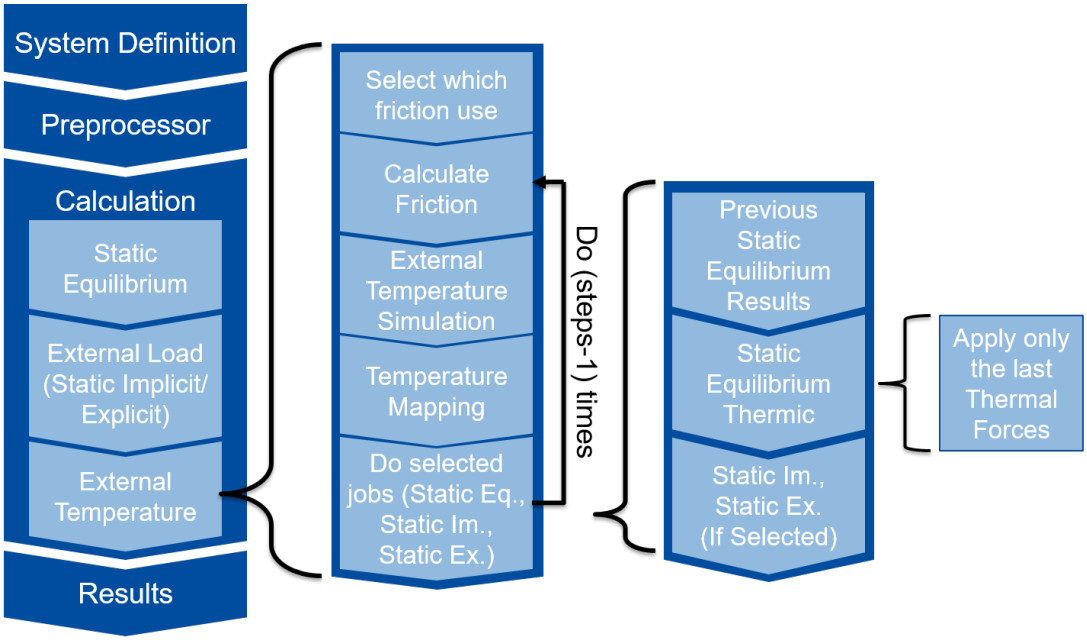

Figure 47 – Updated Heat working flow.

Source – Original.

In the *Static Equilibrium* performed in the UH approach only the *Static Equilibrium Thermic* (Figure 10) will be performed, using only the last Thermic Load Substitutes column as a load input. Since the thermal forces are added in the system before the external load, the *Static Implicit* and *Static Explicit* jobs needs to be fully calculated using the new *Static Equilibrium* calculated.

The thermal model results are stored and used as an input for the next iteration. Thus, in the case that the *Experimental Data* is used for the friction input, the thermal model results are the same, otherwise, if the *MTPlus Data* is used as friction input, the thermal forces will change the contact characteristics of the rolling elements, resulting in a new friction value and in a distinct result for the thermal model.

Regarding the mechanical model, in the UH the thermal forces will be applied in steps into the system, resulting in a difference in the contact characteristics and displacement. However, being the temperature difference small, the final mechanical results between the UH and NUH are slightly different.

6.5 COUPLING RESULTS

With all the presented modifications on the mechanical model, the calculated displacement results, for a shaft rotational speed of 500 RPM, with a thermal model simulation time of 3 hours, using the Stribeck Curve measured as the nut-screw interface friction torque, the Weighted Mean V2 as the thermal mapping approach and the NUH as the thermal-mechanical coupling; is compared against the measured data on

the test rig. The validation of the thermal-mechanical coupling with the friction models results was not carried out due to the fact that the friction models calculation at 500 RPM are quite different from the Stribeck Curve measured. The external load applied in the test nut was from 1000 N until 6000 N in steps of 1000 N.

The Stribeck Curve was measured without any external load applied on the nuts, but it can be used for the cases where the load is applied by the fact that on the measured data the thermal increase with and without external load applied are almost identical.

In Figure 48 are presented the measured data and calculated results for the test nut displacement when there is no thermal delta in the components and with a thermal delta resultant of 3 hours thermal simulation.

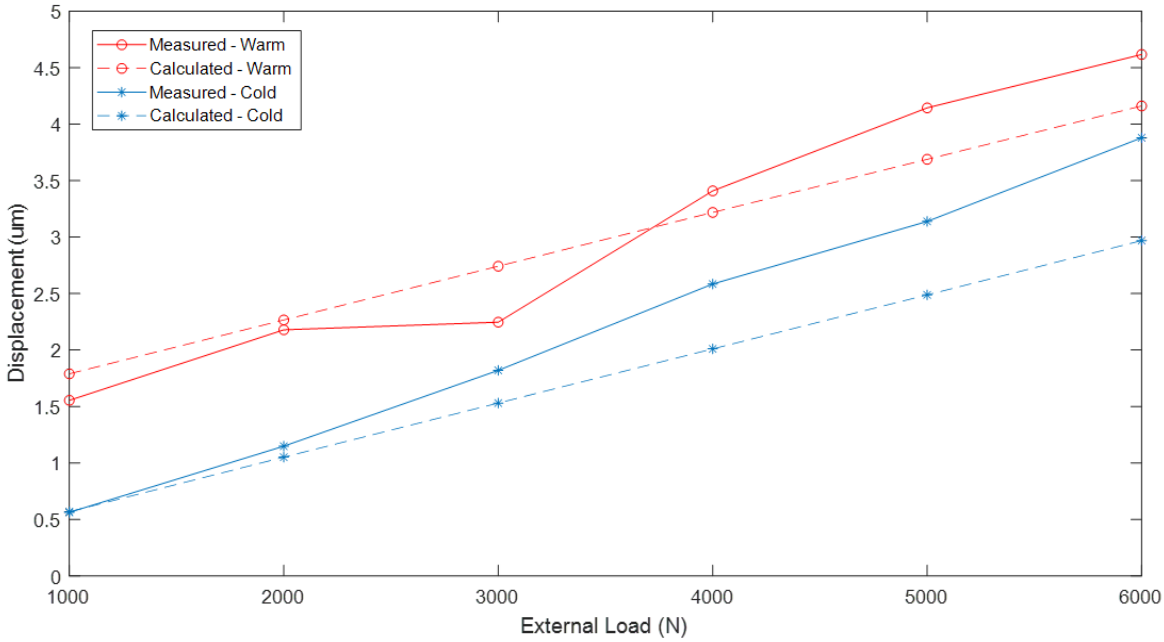

Figure 48 – Axial Displacement - Measured and Calculated.

Source – Original.

The values from Figure 48 and the perceptual deviation between the measured and calculated results are available in Table 10.

For the Cold results shown in Table 10 the displacement deviations are similar to the prior model developed. This is explained by the fact that in this work the MTPlus calculation for no thermal influence was not changed. Concerning to the Warm results the absolute mean of the displacement deviations is equal to 11.27 %. On previous model, this value was equal to 70.57 %. Thus, the work developed in this project brings an improvement to the mechanical model calculation.

The temperature of the FEA elements on the MTPlus can be visualized in Figure 49. The highest temperatures on the system are found nearby the fixed bearing. On

		Cold			Warm	
Load	Measured	Calculated	Deviation	Measured	Calculated	Deviation
6000 N	3.88 µm	2.97 µm	-23.48%	4.62 µm	4.16 µm	-9.87%
5000 N	3.14 µm	2.49 µm	-20.73%	4.14 µm	3.69 µm	-10.99%
4000 N	2.58 µm	2.01 µm	-22.22%	3.41 µm	3.22 µm	-5.60%
3000 N	1.82 µm	1.53 µm	-15.91%	2.25 µm	2.74 µm	22.06%
2000 N	1.19 µm	1.05 µm	-8.47%	2.18 µm	2.27 µm	3.99%
1000 N	0.56 µm	0.57 µm	-1.08%	1.55 µm	1.78 µm	15.12%

Table 10 – Displacement Values and Perceptual Deviation

Source – Original

the middle of the spindle length a local temperature maximum occurs, due to the travel length of the nuts on the thermal model.

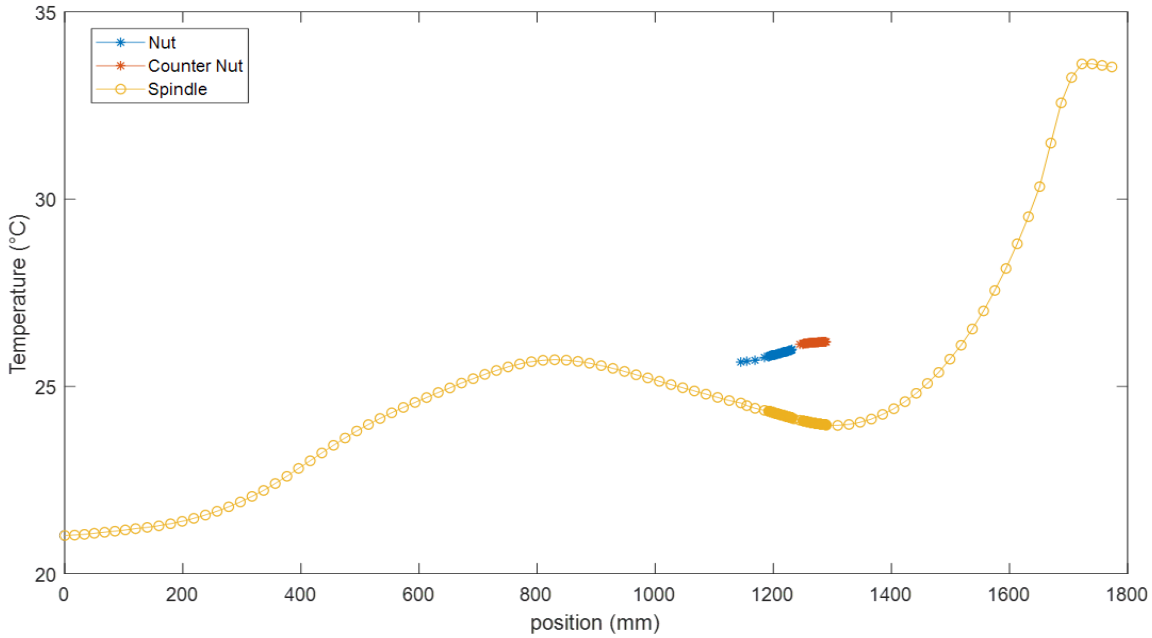

Figure 49 – Temperature of the MTPlus components over the length.

Source – Original.

As the spindle temperature is lower than the nut and counter nut temperature, on the position where the nut system is placed, the thermal forces acting on the nuts are higher than the ones acting in the spindle, resulting that the axial displacement will be higher in the nuts than in the same length of the spindle. Due to this, as already shown in Figure 48, the displacement calculated and measured will be higher after the working time.

As part of the contact characteristics calculated on MTPlus, in Figure 50 are displayed the contact pressure at the ball screw groove contact of each rolling element for no thermal delta between the components and with a thermal delta generated by

the *Constant External Temperature*.

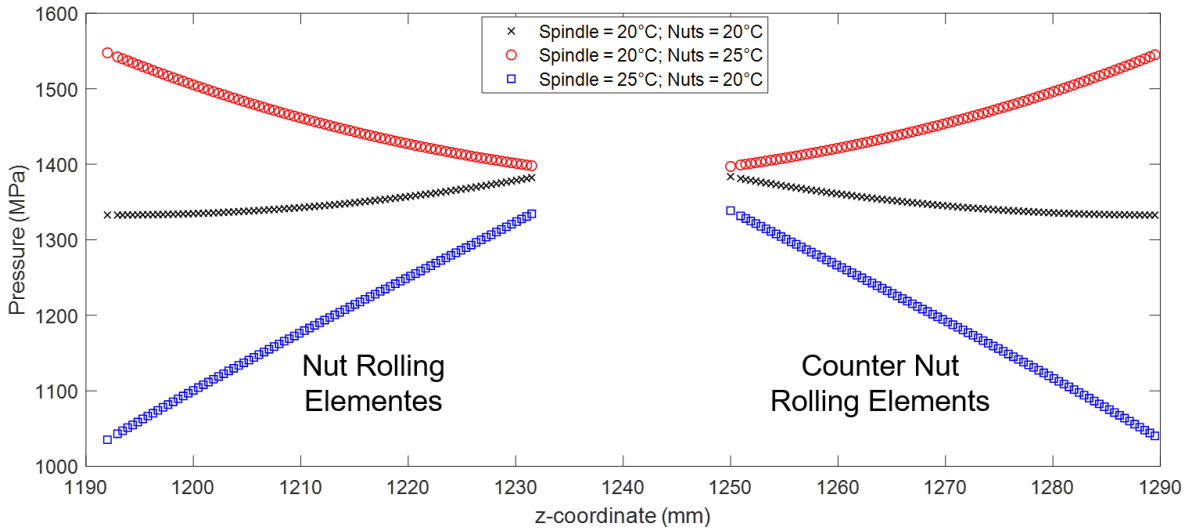

Figure 50 – Contact Pressure for Multiples Components Temperatures.

Source – Original.

For the case where the components have the same temperature the only force acting in the system is the preload. The contact pressure on the rolling elements nearby the spring that generates the preload (position 1231 mm and 1250 mm) is the higher one. As far from these positions, smaller will be the contact pressure. When the temperature of the spindle is higher than the nut, thermal expansion will occur on the spindle elements, so the nut and spindle grooves displacement as shown in Figure 6b will decrease as far as it goes from the spring, resulting in a lower contact pressure on the rolling elements. The opposite is true, with higher temperature on the nut, the nut and spindle grooves displacement increase, resulting in higher contact pressure action on the rolling elements.

To analyse the contact pressure with the thermal model temperatures previous presented multiples nuts travel position was considered and are displayed on Figure 51.

Concerning to Figure 51 it is important to mention that on the MTPlus the components do not change position during the calculation, the presented position was changed on the MTPlus configurations. Since the friction used is the experimental data, the thermal results of each calculation will be the same.

With these thermal delta between the components, on Figure 52 is displayed the pressure at the ball screw groove contact for the multiples positions at Figure 51.

When the nut is at the start position the thermal delta between the nut and counter nut to the spindle is higher, thus, the pressure at the rolling element would be higher too. At the end position, the temperature difference between nut and counter nut to the spindle is almost constant at the rolling elements positions. This thermal

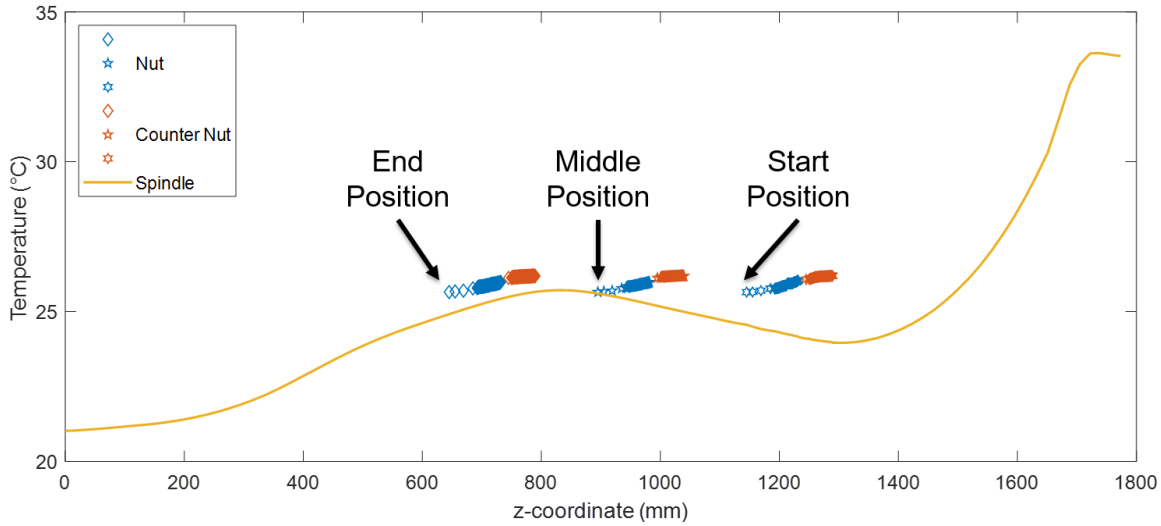

Figure 51 – Multiples Nut Position at MTPlus.

Source – Original.

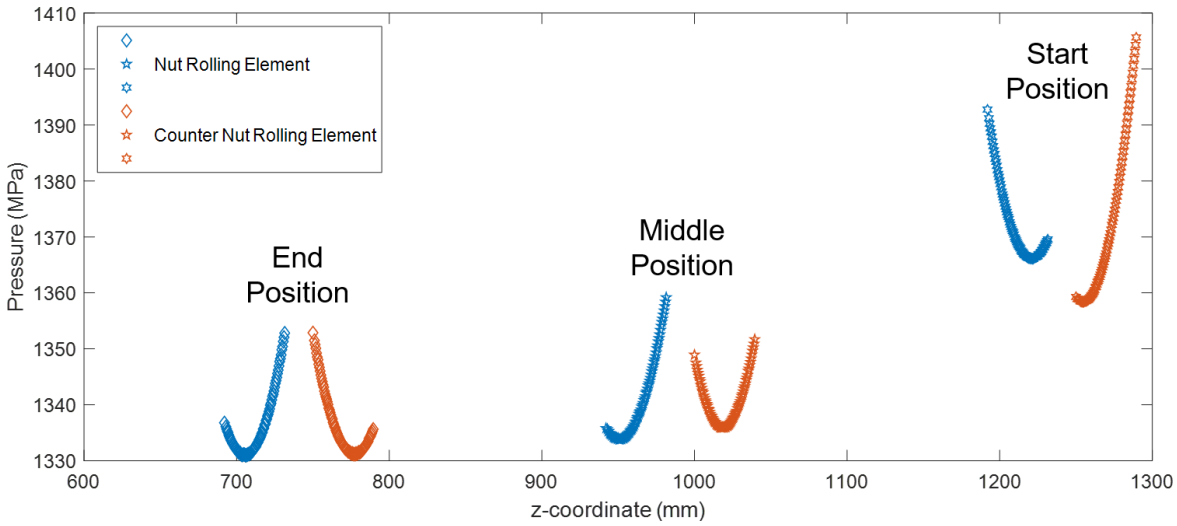

Figure 52 – Contact Pressure at Multiples Nuts Position.

Source – Original.

difference is lower than the difference visualized at the start position, therefore, the contact pressure would be lower.

At the middle position of the travel length the thermal difference has the same shape as at the start position regarding the fact that the value of this delta will be lower. The pressure delta between the last rolling element of the nut and the first rolling element of the counter nut is more like the start position than the end position. Otherwise, by the fact that the thermal delta is not so high as in the start position, the overall slope is more like the end position. At the nut the first rolling element has a pressure lower than the same element at the end position, but the last element of the

nut have a higher pressure. The behavior of the counter nut rolling elements is a mix of the ones at the end and start position, as the pressure at the last rolling element is higher than the first one, but this difference is not so large as what happens on the start position.

7 CONCLUSION AND OUTLOOK

Since multiples steps were involved in the whole project, the overview will be made individually for each one.

- **Mechanical Model:** Regarding the mechanical model the Friction models implemented do not give a result close to the measured data. The parametric values of both models needs to be better selected, mostly in the EHD calculation parameters, considering that the biggest divergences between the results are in higher speeds, where the EHD friction have a higher influence than the CSB. Since Steinert divides the components of the friction between EHD and CSB, the study of the behavior of the components due the changes of the speed is simpler than the Olaru et al. (2005) model. For future works both models implementation needs to be improved, being a suggestion for the Steinert Model using on the ball screw calculation to be implemented a ball to ball friction as presented by Olaru et al. (2005), but keeping distinction between the kind of friction (EHD and CSB). In the Steinert Model a friction between the ball and the cage exist, but was not implemented in this work, perhaps, for future works, it should be implemented, with some considerations, to try to fill the gap of the ball to ball friction.
- **Thermal Model:** the thermal model results achieved are great, most of results compared to the test rig data stay in the acceptable range of the R^2 Performance Index, and the ones that do not stay in the acceptable range of the R^2 are or of low importance for the coupling (Loose Bearing) or was affected by measurement issued (Thermal Camera Moving).
- **Models Coupling:** the thermal model to the mechanical model coupling was validated and the achieved results for the displacement are better than the results of the previous work developed. The connection from the mechanical model to the thermal model is implemented, but since the friction models give results unsuitable when compared to measured data, it was not possible to validate the connection.

Regarding to the goals on the section 1.1 the following comments are relevant:

- **Verify and validate the thermal model:** the thermal model was improved and it results was validated for two different operations speeds.
- **Create a compatibility layer between the models:** four different mapping approaches were discussed on this project.
- **Interconnect both models:** the use of the thermal model results on the mechanical model was implemented and validated, otherwise, since the frictions values

calculated do not fit the Stribeck Curve measured, the mechanical model results was not used on the thermal model.

- **Validate the simulation results against experimental data:** The thermal model result was validated against the PT100 and the Thermal Camera measurements. The mechanical model displacement calculated was validated against the LVDT measurements with a thermal delta due to the working time.

REFERENCES

ALBERICH-BAYARRI, A.; MORATAL, D.; MARTI-BONMATI, L.; SALMERON-SANCHEZ, M.; VALLES-LLUCH, A.; NIETO-CHARQUES, L.; RIETA, J. J. Volume Mesh Generation and Finite Element Analysis of Trabecular Bone Magnetic Resonance Images, p. 1603–1606, 2007. DOI: 10.1109/IEMBS.2007.4352612.

ALTINTAS, Y.; VERL, A.; BRECHER, C.; URIARTE, L.; PRITSCHOW, G. Machine tool feed drives. **CIRP Annals**, v. 60, n. 2, p. 779–796, 2011. ISSN 0007-8506. DOI: https://doi.org/10.1016/j.cirp.2011.05.010. Available from: http://www.sciencedirect.com/science/article/pii/S0007850611002125.

AUTODESK. **Beam Elements**. Available from: http://download.autodesk.com/us/algor/userguides/mergedProjects/setting_up_the_analysis/linear/Elements/Beam_Elements.htm. Visited on: 24 Aug. 2020.

AUTODESK. **Tetrahedral Elements**. Available from: http://download.autodesk.com/us/algor/userguides/mergedProjects/setting_up_the_analysis/linear/Elements/Tetrahedral_Elements.htm. Visited on: 24 Aug. 2020.

BARNES INDUSTRIES, Inc. **How A Ball Screw Works**. Available from: http://www.barnesballscrew.com/how-a-ball-screw-works/. Visited on: 19 Aug. 2020.

BATCHU, S. **Beam and Bar Elements**. Available from: https://www.stressebook.com/beam-and-bar-elements/. Visited on: 24 Aug. 2020.

BENINCÁ, I. **A Thermal Elastic Model for Ball Screw**. 2019. Diplomarbeit – Rheinisch-Westfälische Technische Hochschule Aachen, Aachen, North Rhine-Westphalia - Germany.

BRECHER, C.; ESSER, B.; FALKER, J.; KNEER, F.; FEY, M. Modelling of ball screw drives rolling element contact characteristics. **CIRP Annals**, v. 67, n. 1, p. 409–412, 2018. ISSN 0007-8506. DOI: https://doi.org/10.1016/j.cirp.2018.04.109. Available from: http://www.sciencedirect.com/science/article/pii/S0007850618301331.

CAZZANIGA, P.; NOBILE, M. S.; BESOZZI, D. The impact of particles initialization in PSO: Parameter estimation as a case in point, p. 1–8, 2015. DOI: 10.1109/CIBCB.2015.7300288.

COELHO, A.; COELHO, L. **Identificação de sistemas dinâmicos lineares.** Florianópolis, Santa Catarina - Brasil: Edufsc, 2004. v. 2.

COOK, R. D.; MALKUS, D. S.; PLESHA, M. E.; WITT, R. J. **Concepts and applications of finite element analysis**. 4th ed. New York, NY: Wiley, 2001. ISBN 0-471-35605-0.

FALKER, J. **Analyse des Betriebsverhaltens von Hochgeschwindigkeits-Wälzlagern unter radialen Lasten**. [S.l.]: Apprimus Wissenschaftsverlag, 2020. ISBN 9783863598174. Available from: https://books.google.de/books?id=XJLLDwAAQBAJ.

FLETCHER, S.; FORD, D.G. Measuring and modelling heat transfer and thermal errors on a ballscrew feed drive system. **WIT Transactions on Engineering Sciences**, v. 44, p. 349–360, 2003. DOI: 10.2495/LAMDAMAP030301. Available from: https://www.witpress.com/elibrary/wit-transactions-on-engineering-sciences/44/13943.

GOBIN, A.; PEROT, T. **Determination of the critical Rayleigh number**. 1999. Available from: http://hmf.enseeiht.fr/travaux/CD9900/travaux/optmfn/gpfmho/99-00/grp13/chap2.htm. Visited on: 15 Nov. 2020.

GOHAR, R. Oil Film Thickness and Rolling Friction in Elastohydrodynamic Point Contact. **Journal of Lubrication Technology**, v. 93, n. 3, p. 371–379, July 1971. ISSN 0022-2305. DOI: 10.1115/1.3451598. eprint: https://asmedigitalcollection.asme.org/tribology/article-pdf/93/3/371/5513733/371_1.pdf. Available from: https://doi.org/10.1115/1.3451598.

GOHAR, R.; RAHNEJAT, H. **Fundamentals of Tribology**. 3rd. [S.l.]: WORLD SCIENTIFIC (EUROPE), 2018. DOI: 10.1142/q0152. eprint: https://www.worldscientific.com/doi/pdf/10.1142/q0152. Available from: https://www.worldscientific.com/doi/abs/10.1142/q0152.

HUTTON, D. V. **Fundamentals of Finite Element Analysis**. [S.l.]: McGraw-Hill, 2003. (Engineering Series). ISBN 9780072922363. Available from: https://books.google.de/books?id=CV2HLsuNMtsC.

KAWAKAMI, K.; MENG, Zhi. Improvement of Particle Swarm Optimization. **Piers Online**, v. 5, p. 261–264, Jan. 2009. DOI: 10.2529/PIERS080908052538.

KENNEDY, J.; EBERHART, R. Particle swarm optimization. v. 4, 1942–1948 vol.4, 1995.

MARION, Glenn; LAWSON, Daniel. **An Introduction to Mathematical Modelling**. Available from: https://people.maths.bris.ac.uk/~madjl/course_text.pdf. Visited on: 18 Aug. 2020.

NSK. **Chapter 2 Construction of Ball Screws and Their Functional**. English. Version 2.2.x. [S.l.], Nov. 2011.

OLARU, D.; PUIU, G.; BALAN, L. C.; PUIU, V. A New Model to Estimate Friction Torque in a Ball Screw System. **Product Engineering: Eco-Design, Technologies and Green Energy**, p. 333–346, Jan. 2005. DOI: 10.1007/1-4020-2933-0_20.

OYANGUREN, A.; LARRAÑAGA, J.; ULACIA, I. Thermo-mechanical modelling of ball screw preload force variation in different working conditions. **The International Journal of Advanced Manufacturing Technology**, Springer Nature, v. 97, n. 1-4, p. 723–739, Apr. 2018. DOI: 10.1007/s00170-018-2008-8.

PENTENRIEDER, B. **Finite Element Solutions of Heat Conduction Problems in Complicated 3D Geometries Using the Multigrid Method**. 2005. Diplomarbeit – Technische Universität München, München, Bayern - Germany.

PLATH, Dipl.-Des. Heike Iris. The Future of Production Engineering, WZL in Profile. English. [S.l.], Nov. 2019. Available from: https://www.wzl.rwth-aachen.de/global/show_document.asp?id=aaaaaaaaaouwywq&download=1.

RAHMAN, R.; TAMIN, N.; KURDI, O. Stress analysis of heavy duty truck chasis as a preliminary data for its fatigue life prediction using FEM, Dec. 2008.

ROBINSON, J.; ZHOU, Y.; BHATTACHARYA, P.; ERCK, R.; QU, J.; BAYS, J.; COSIMBESCU, L. Probing the molecular design of hyper-branched aryl polyesters

towards lubricant applications. **Scientific Reports**, v. 6, p. 18624, Jan. 2016. DOI: 10.1038/srep18624.

ROCHA, L. **Simulation-based optimization of a precision glass molding thermal model**. 2020. Diplomarbeit – Rheinisch-Westfälische Technische Hochschule Aachen, Aachen, North Rhine-Westphalia - Germany.

ROHSENOW, Warren M.; HARTNETT, James P.; CHO, Young I., et al. **Handbook of heat transfer**. USA: McGraw-Hill New York, 1998. v. 3.

STEINERT, Thomas. **Das Reibmoment von Kugellagern mit bordgefuhrtem Käfig**. 1995. Phd's Thesis – Rheinisch-Westfälische Technische Hochschule Aachen, Aachen, North Rhine-Westphalia - Germany.

TÜLLMANN, U. **Das Verhalten axial verspannter, schnelldrehender Schrägkugellager**. 1999. Phd's Thesis – Rheinisch-Westfälische Technische Hochschule Aachen.

VEREIN DEUTSCHER INGENIEURE. **VDI-Wärmeatlas**. Ed. by VDI e.V. 11. ed. Berlin Heidelberg: Springer, 2013. (VDI-Buch). ISBN 978-3-642-19980-6. DOI: 10.1007/978-3-642-19980-6.

VERL, A.; FREY, S. Correlation between feed velocity and preloading in ball screw drives. **CIRP Annals**, v. 59, n. 1, p. 429–432, 2010. ISSN 0007-8506. DOI: https://doi.org/10.1016/j.cirp.2010.03.136. Available from: http://www.sciencedirect.com/science/article/pii/S000785061000137X.

WÄLZLAGER Katalog. Deutschland: Schaeffler Technologies GmbH & Co. KG, 2014.

ZHOU, R. S.; HOEPRICH, M. R. Torque of Tapered Roller Bearings. **Journal of Tribology**, v. 113, n. 3, p. 590–597, July 1991. ISSN 0742-4787. DOI: 10.1115/1.2920664. eprint: https://asmedigitalcollection.asme.org/tribology/article-pdf/113/3/590/5501459/590_1.pdf. Available from: https://doi.org/10.1115/1.2920664.